

THESIS FOR THE DEGREE OF LICENTIATE OF ENGINEERING

Structure and chemical ordering in metallic nanoparticles from atomic scale modeling

J. MAGNUS RAHM

Department of Physics

CHALMERS UNIVERSITY OF TECHNOLOGY

Göteborg, Sweden 2019

Structure and chemical ordering in metallic nanoparticles from atomic scale modeling
J. MAGNUS RAHM

© J. Magnus Rahm, 2019

Department of Physics
Chalmers University of Technology
SE-412 96 Göteborg, Sweden
Telephone +46 (0)31 772 10 00

Cover: Rendition of an icosahedron with two tetrahedral crystals partially detached.

Chalmers reproservice
Göteborg, Sweden 2019

Structure and chemical ordering in metallic nanoparticles from atomic scale modeling

J. MAGNUS RAHM
Department of Physics
Chalmers University of Technology

Abstract

In the last decades, a wide range of attractive properties have put metallic nanoparticles in the spotlight. These properties, often related to optical response and catalytic performance, are to a large extent dependent on structure and chemical ordering, that is, the distribution of elements in the nanoparticle. To better understand and predict the behavior of such particles, a thorough understanding of these parameters is essential. This thesis investigates structure and chemical ordering in metal nanoparticles using atomistic modeling based on molecular dynamics and Monte Carlo simulations with embedded atom method potentials. The thesis describes frequently occurring nanoparticle structures and discusses the importance for an atomistic perspective in relation to the existence of magic and non-magic numbers in particles with different shapes. Further, alloy thermodynamics and key differences and similarities between macroscopic and microscopic systems are reviewed from a statistical mechanics perspective. The thesis highlights the importance for comprehensive investigations of the size and composition parameters to obtain a coherent picture. In particular, it is shown how recognition of polydisperse nanoparticle ensembles is crucial to predict the distribution of nanoparticle shapes in thermodynamic equilibrium and how the distribution of elements in an alloy nanoparticle is intimately connected to the underlying structure.

Keywords: nanoparticles, nanoparticle shapes, nanoparticle structures, icosahedron, Marks decahedron, regular truncated octahedron, chemical ordering, molecular dynamics, Monte Carlo, modeling

LIST OF APPENDED PAPERS

This thesis is partially based on work presented in the following papers:

I Beyond Magic Numbers: Atomic Scale Equilibrium Nanoparticle Shapes for Any Size

J. Magnus Rahm and Paul Erhart
Nano Letters, 17, 5775–5781 (2017)

II Understanding Chemical Ordering in Bimetallic Nanoparticles from Atomic-Scale Simulations: The Competition between Bulk, Surface, and Strain

J. Magnus Rahm and Paul Erhart
The Journal of Physical Chemistry C, 122, 28439–28445 (2018)

The author's contribution to the papers:

- I The author refined the algorithm, carried out the simulations, analyzed the results, and wrote a first draft of the paper.
- II The author carried out the majority of the simulations, analyzed the results, and wrote a first draft of the paper.

PUBLICATIONS NOT INCLUDED IN THIS THESIS

The following publications are outside the scope of this thesis:

ICET – A Python library for constructing and sampling alloy cluster expansions

Mattias Ångqvist, William A. Muñoz, J. Magnus Rahm, Erik Fransson, Céline Durniak, Piotr Rozyczko, Thomas Holm Rod, and Paul Erhart
arXiv preprint arXiv:1901.08790 (2019)

Contents

1	Introduction	1
1.1	Structure of the thesis	2
2	Shapes and structures of nanoparticles	3
2.1	A simple model for the energy	3
2.2	The Wulff construction	4
2.3	Nanoparticle shapes	5
2.3.1	Truncated octahedra	6
2.3.2	Truncated decahedra	6
2.3.3	Icosahedra	7
2.3.4	Other shapes	8
2.4	Comparison of energetics	8
2.5	Deficiencies of continuum models	9
3	Thermodynamics of metallic alloys	11
3.1	Phase diagrams	11
3.2	Mean field treatment of the Ising model	12
3.3	Order and disorder	14
3.4	Chemical order in nanoalloys	15
4	Statistical mechanics at the bulk and nanoscale	19
4.1	Statistical mechanics in the thermodynamic limit	19
4.2	Small systems	20
4.3	Ensembles of nanoparticles	22
5	Computational methods	25
5.1	The Born–Oppenheimer approximation	25
5.2	Interatomic potentials	26
5.2.1	Embedded atom method	26
5.3	Atomistic simulations	28
5.3.1	Molecular dynamics	28

5.3.2	Time and ensemble averages	28
5.3.3	Monte Carlo simulations	29
5.3.4	The semi-grand canonical ensemble	29
5.3.5	The variance-constrained semi-grand canonical ensemble	31
5.3.6	Hybrid MD–MC simulations	31
5.4	Energy minimization techniques	32
5.4.1	Spatial and configurational global optimization	32
5.4.2	Local optimization	33
5.4.3	Simulated annealing	34
5.5	Elastic strain	34
6	Summary of the papers	35
6.1	Paper I	35
6.2	Paper II	36
7	Outlook	37
A	Decahedral and icosahedral geometry	39
A.1	The decahedron	39
A.2	The icosahedron	41
	Acknowledgments	43
	Bibliography	45
	Papers I-II	55

Introduction

When Lemuel Gulliver finds himself washed ashore the country of Lilliput in Jonathan Swift's famous novel from 1726, he never explicitly reflects on the exceptional surface-to-volume ratio of its inhabitants. If he had, he would have been a pioneer in recognizing one of the most important reasons for the remarkable properties exhibited by objects at small scales, most notably nanoparticles. But high surface-to-volume ratio is just as meager a description of nanoparticles as it is of Lilliputians. Nanoparticles come in countless structures and shapes, they are made of a wide range of materials, and they are mono-elemental or mixed, with different compositions and configurations. This rich diversity coupled with quantum mechanics and, indeed, high surface-to-volume ratio, gives rise to an extraordinary range of intriguing properties and applications.

One may say that the history of nanoscale inventions began more than a thousand years ago, although the practitioners, who colorized cups, pots and windows, did not know the length scale of the materials they used. Prominent contributions were made by Michael Faraday and others already in the 19th century [1], but the age of nanotechnological enlightenment started in the second half of the 20th century. After some decades of intense research, nanomaterials have now found their way into numerous applications, ranging from medicine [2] via sunscreen [3] to tennis rackets [4].

For metallic nanoparticles specifically, much of academic and commercial interest can be attributed to optical properties. The combination of conduction electrons and a geometry smaller than the wavelength of light gives rise to plasmonic resonance, which renders the optical response of nanoparticles completely different from the same materials in bulk. Metallic nanoparticles are also in focus for many applications in heterogeneous catalysis, where the high surface-to-volume ratio helps boosting the activity. Optical response and catalytic activity are but two examples of properties that are dependent on shape and, in the case of alloy nanoparticles (nanoalloys), the distribution of the elements in the particles, here referred to as chemical ordering. To

properly predict and explain the behavior of nanoparticles one is thus often forced to take these aspects into account. The great variety of nanoparticles made of different materials and in different ways renders this task a complicated puzzle. This thesis aims to contribute a few more pieces for a more coherent picture to emerge. The focus of the thesis is structure and chemical ordering in metallic nanoparticles in thermodynamic equilibrium using atomistic modeling, primarily molecular dynamics (MD) and Monte Carlo (MC) simulations based on interatomic potentials.

1.1 Structure of the thesis

An introduction to nanoparticle structures and shapes is given in Chapter 2, along with some considerations on when atomistic models are required. The thermodynamics of alloys in the bulk and at the nanoscale is introduced in Chapter 3. The limits of thermodynamics at the nanoscale and some key differences between macroscopic and microscopic systems are discussed in Chapter 4 with the aid of statistical mechanics. Chapter 5 describes the computational methods used in the papers. Finally, the two papers included in the thesis are summarized in Chapter 6 and a brief outlook is provided in Chapter 7.

Shapes and structures of nanoparticles

They say no two snowflakes are alike, but the same statement would not be true for metallic nanoparticles. Being made of materials that are crystalline at room temperature, they tend to form highly regular structures that usually can be categorized as shapes well-known from fundamental geometry. This chapter explains the emergence of these particle shapes from a continuum perspective and discusses when the continuum approach needs to be replaced by a model with atomistic resolution.

2.1 A simple model for the energy

The shapes of nanoparticles are governed by the energetics of the materials of which they are made. The total energy of a nanoparticle may, as a first approximation, be written as a polynomial in the particle volume V ,

$$E_{\text{nanoparticle}} = aV + bV^{2/3} + cV^{1/3} + d. \quad (2.1)$$

The first term incorporates all contributions that scale with the volume of the particle, including cohesive energy and strain. The second term, $bV^{2/3}$, includes the energy of the surface and any other contributions that scale with area. The third term, $cV^{1/3}$, accounts for linear defects such as edges. The fourth term, d , is made up of any zero-dimensional contribution, including corners and point defects. The coefficients are themselves functions of the shape of the particle. A cube, for example, has edges and corners whereas a sphere does not, and hence we expect c and d to be much larger for the cube than the sphere.

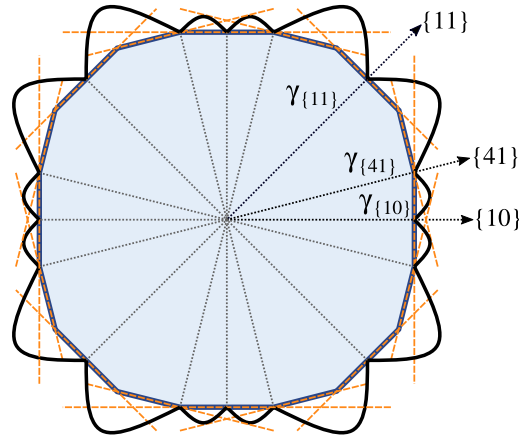


Figure 2.1: Wulff construction in two dimensions. The distance from the origin to the thick black line is proportional to the surface energy for a surface with that crystal orientation. In this hypothetical example, three inequivalent facets are exposed in the optimal shape (filled with blue), namely $\{10\}$, $\{11\}$ and $\{41\}$.

To find the equilibrium nanoparticle shape we need to find the shape whose coefficients minimize Eq. (2.1) for a given volume. For water or any other liquid, this problem is trivial; the lowest energy shape is always a sphere because a sphere has the smallest possible surface area for a given volume (edges and corners will always add positive contributions). For crystals, however, the problem is far from trivial, because the surface energy of a crystal is facet dependent, i.e., it depends on the orientation of the surface. Also, a crystal may be strained and incorporate defects that will contribute to any of the coefficients a , b , c or d depending on its dimensionality. This gives rise to a rich variety of particle structures, which are stable at specific sizes in specific materials. The situation calls for refined models in which the effects of crystallinity are accounted for.

2.2 The Wulff construction

The Wulff construction [5, 6] solves the problem of finding the optimal particle shape given a set of surface energies. Wulff constructions are based on polar plots of surface energy, where the distance from the origin in a certain direction is proportional to the surface energy of a facet with that orientation. Planes are drawn perpendicular to a vector from the origin to each point in each direction, and the optimal shape is finally obtained as the inner envelope of such planes. The procedure is outlined in Fig. 2.1 for a two dimensional case. From this construction, one realizes that the surface of a

particle will be dominated by low energy facets.

Although the mathematical subtleties led Wulff himself to give an incomplete proof of the construction, a motivation for its validity can be given in simple terms [7]. Consider a set of surface energies γ_i . With distances h_i from the origin to each facet, and with corresponding facet areas A_i , we can write the total surface energy as

$$E_{\text{surface}} = \sum_i \gamma_i A_i \quad (2.2)$$

and the volume of the particle as

$$V = \sum_i \frac{1}{3} h_i A_i. \quad (2.3)$$

We want to minimize the total surface energy for a fixed volume V_0 . The latter condition can be handled with a Lagrange multiplier,

$$\delta [E_{\text{surface}} - \lambda(V - V_0)] = \sum_i \delta \left(\gamma_i A_i - \lambda \frac{1}{3} h_i A_i \right) = 0 \quad (2.4)$$

where the variation vanishes for the minimum energy shape. The method of Lagrange multipliers asserts that the terms vanish independently, so that

$$h_i \propto \gamma_i \quad (2.5)$$

with the same constant of proportionality for all facets i . This is the condition required by the Wulff construction.

2.3 Nanoparticle shapes

The Wulff construction requires facet-dependent surface energies as input. Surface energies as calculated with the interatomic potentials¹ employed in Paper I and II are visualized in Fig. 2.2. We can rationalize the results by a simple bond-counting model; facets that minimize the number of broken bonds also have the lowest energies, which typically means that the close-packed $\{111\}$ surface is the lowest energy facet in face-centered cubic (FCC) metals such as Au. Among low-index facets, $\{100\}$ and $\{110\}$ usually follow and all other facets are irrelevant for the Wulff construction in the sense that they are not exposed in the lowest energy shape². This section introduces some shapes that are primarily relevant for materials in which the $\{111\}$ facet has the lowest energy.

¹These surface energies are generally lower than the experimentally observed values. This disagreement is a consequence of the interatomic potentials being fitted to DFT data obtained using functionals that often underestimate surface energies [11], most notably PBE [12].

²This is an idealized description. In reality, $\{100\}$ and $\{110\}$ facets often reconstruct.

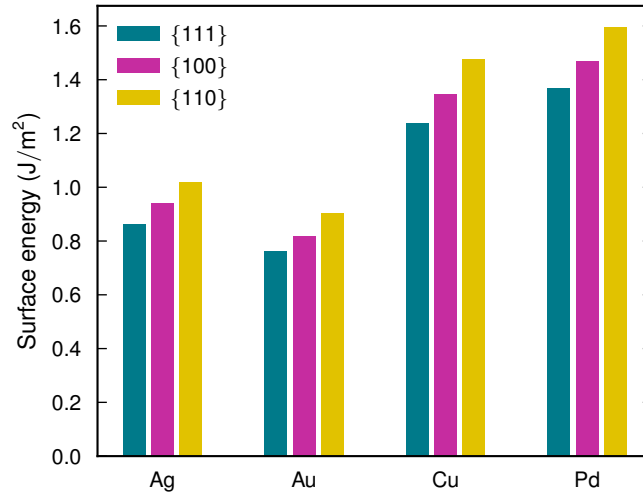


Figure 2.2: Surface energies for four late transition metals calculated with the EAM potentials parametrized by Mishin *et al.* for Cu [8], Williams *et al.* for Ag [9] and Marchal *et al.* for Au and Pd [10].

2.3.1 Truncated octahedra

The Wulff construction resulting from the surface energies for Au from Fig. 2.2 can be described as a truncated octahedron [Fig. 2.3(a)]. The lowest energy facet, {111}, does indeed have the largest area, followed by {100} and {110}. Note that a complete (not truncated) octahedron has only {111} facets, but according to the Wulff construction, it is still not the lowest energy structure because of its high surface-to-volume ratio. In this thesis, octahedra that are truncated such that the hexagonal {111} facets are equilateral (disregarding {110}) will be referred to as regular truncated octahedra (RTOs). In the Wulff construction they emerge when

$$\frac{\gamma_{100}}{\gamma_{111}} = \frac{2}{\sqrt{3}} \approx 1.15, \quad (2.6)$$

i.e., when the surface energy of the {100} facet is approximately 15 % larger than the surface energy of {111}.

2.3.2 Truncated decahedra

The (original) Wulff construction assumes a single crystalline particle. If this requirement is relaxed, it is possible to construct particles with lower surface energy than the Wulff shape. Stacking five tetrahedra such that they share an edge [Fig. 2.3(b)] produces

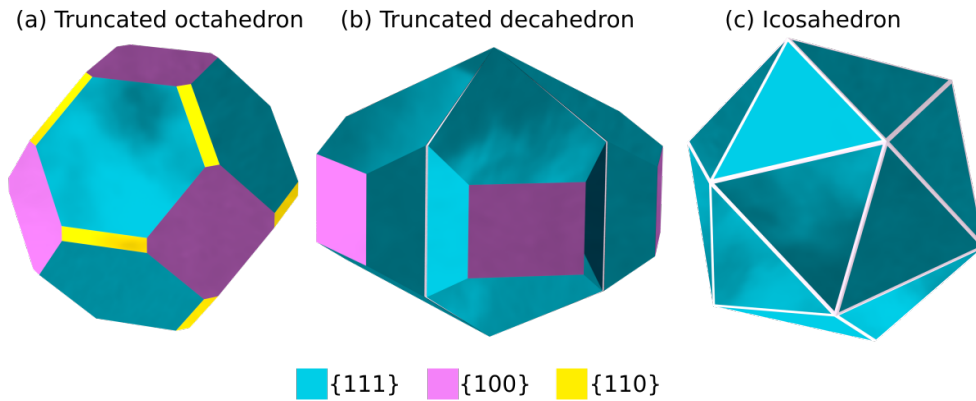


Figure 2.3: Nanoparticle shapes commonly adopted by noble metals: (a) truncated octahedron resulting from a Wulff construction of the surface energies for Ag from Fig. 2.2, (b) Marks decahedron, and (c) icosahedron. The latter two are always strained, because if they were not, gaps corresponding to the grey areas (hardly visible in the decahedron) would be left open.

one such example [13]. This shape, referred to as a decahedron and first observed in experiments on nanoparticles more than 50 years ago [14, 15], exposes nothing but $\{111\}$ facets but contains twin boundaries at the interface between each pair of tetrahedra as well as a line defect where the five tetrahedra meet. In the context of Eq. (2.1), the twin boundaries and line defect will effectively increase the values of b and c , respectively. Furthermore, a decahedron is always strained, because five equilateral tetrahedra do not completely fill space. As shown in Appendix A, if the length of the edges in the center and the length of the edges connecting apex and equator are the same, the edges at the equator will be stretched by approximately 1.8%.

It can be shown with a generalized Wulff construction [16] that truncation of the decahedron yields energies that are lower than the complete decahedron for typical surface energies. Two truncations are usually observed; truncation of the edges of the particle, and notches at the edges where two tetrahedra meet. Both are illustrated in Fig. 2.3(b). The former truncation exposes $\{100\}$ facets whereas the latter exposes $\{111\}$. Structures with notches are commonly referred to as Marks decahedra [17].

2.3.3 Icosahedra

If twenty tetrahedra are stacked such that they meet in the center, they form an icosahedron [Fig. 2.3(c)], which, just as the decahedron, has more than 50 years of history in experiment [14, 15]. An icosahedron is quite spherical³ but contains more twin bound-

³A classic football with hexagonal white and pentagonal black patches is in fact a truncated icosahedron (but tends to be pumped even more spherical with air).

aries and is even more strained than the decahedron. Just as for a decahedron, twenty equilateral tetrahedra do not fill space entirely, which causes strain (see Appendix A for a derivation). Geometry does, however, not require the strain to be uniform. In this work, icosahedral particles have been observed to be compressed in the center but essentially free from strain close to the surface. It seems likely that this is simply the most energetically favorable way to fulfill the geometrical requirements. The tetrahedra have their tip in the center, and the number of atoms per shell increases in proportion to the distance from the center. If the height of the tetrahedron, i.e., the distance from its tip in the center to its face at the surface, is commensurate with the equilibrium lattice parameter, the lattice needs to be stretched about 5.1 % in the direction parallel to the surface, which would imply an approximately uniform strain in the particle. If, on the other hand, the length of the face of the tetrahedron is commensurate with the lattice parameter, then the particle must be compressed about 4.9 % in the radial direction. These 4.9 % may be unevenly distributed, and it should be favorable to compress the lattice primarily close to the center of the particle where the number of atoms per radial distance is the lowest.

2.3.4 Other shapes

In addition to the above described shapes, there are some structures that appear regularly. Particularly common among particles with less than a few hundred atoms are polyicosahedra, which are constructed by stacking smaller regular icosahedra [18, 19]. Another example is the rhombic dodecahedral shape, which emerges from a Wulff construction with a low $\{110\}$ surface energy and thus is likely to occur among body-centered cubic (BCC) metals [6, 20]. Experimentalists also synthesize nanoparticles with a plethora of shapes and structures that are out of equilibrium, including rods, cages, stars and cubes [21, 22, 23, 24, 25]. Since this thesis focuses on equilibrium nanoparticles made of FCC metals with more than a hundred atoms, these shapes will not be discussed further.

2.4 Comparison of energetics

To compare the above mentioned shapes, we may construct a series of atomistic structures with increasing number of atoms attaining the target shape, calculate their energy, and fit Eq. (2.1) to each such series. We may then compare the fits and determine which shapes are stable in which size region (Fig. 2.4). Metals that adopt the FCC structure in the bulk generally exhibit the same trend; icosahedra are stable for the smallest sizes, Marks decahedra in an intermediate size regime, and regular truncated octahedra are stable for all sizes above a certain threshold. This trend is an immediate consequence of the scaling of the terms in Eq. (2.1). The first term dominates for large enough sizes,

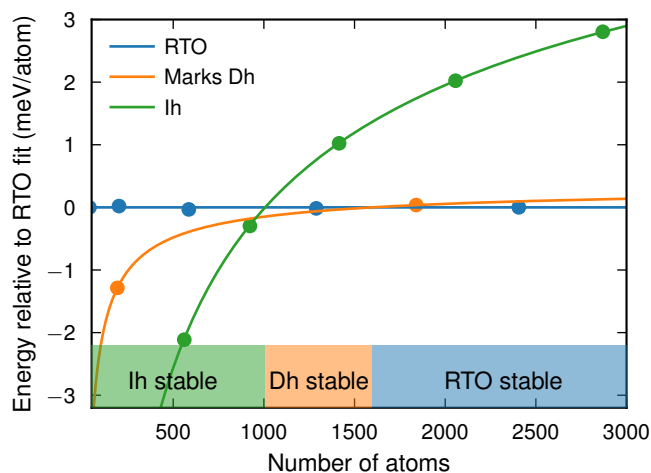


Figure 2.4: Energy per atom in magic number Cu nanoparticles fitted to a third degree polynomial in $N^{-1/3}$ where N is the number of atoms in the particle. The particles were relaxed in LAMMPS [30] with the EAM potential parametrized by Mishin *et al.* [8]. The color bars in the bottom indicate regions of stability, i.e., which shape has the lowest energy.

which destabilizes shapes that are strained, i.e., decahedra and icosahedra. For smaller sizes, the surface-to-volume ratio increases, making the second term increasingly important, favoring particles with a low overall surface energy. Since the icosahedron is more extreme than the decahedron in this sense, for small enough sizes the icosahedron will always be the most stable in this model. This trend is well-established and has been demonstrated by similar means in several publications [26, 27, 28, 29].

2.5 Deficiencies of continuum models

Even though polynomial fits and Wulff constructions are powerful for making general predictions and explain trends, they are fundamentally continuum models and thus inherently unable to account for the finer details of the atomic scale. These include finite size effects pertaining to quantum mechanics, such as the distribution of charge around edges and corners. Volume dependent strain fields caused by surface tension are also lacking in the continuum models described here.

Another important deficiency is that a certain number of atoms cannot form any shape. To create a RTO, for example, one needs 38, 201, 586 (etc.) atoms, and an icosahedron requires 55, 147, 309, 568 (etc.) atoms (marked with circles in Fig. 2.4). These atom counts are referred to as magic numbers. Any number of atoms that does not

match a magic number will always result in a shape that is not ideal, which could mean, for example, a non-equilateral hexagon, an elongated shape, a reconstructed surface or any other defect. In any case, such a particle cannot be expected to be well described by a polynomial fit to magic number particles but will most likely have an energy higher than such a fit. This issue is addressed in Paper I.

To improve the description of the energetics of nanoparticles, one is forced to abandon continuum models and calculate energies on the atomic scale. Atomic scale modeling is the subject of Chapter 5.

Thermodynamics of metallic alloys

It is ancient wisdom that an alloy of two metals often has the favorable properties of both of its components. This is no less true at the nanoscale. The configuration of chemical species, here referred to as chemical ordering, introduces an additional knob that may be turned until a desired property is reached. The knob must, however, obey thermodynamics. This chapter gives an introduction to alloy thermodynamics, beginning with the bulk and closing with implications at the nanoscale.

3.1 Phase diagrams

Information about equilibrium states under various conditions can be visualized in a phase diagram. This section focuses on the special case of a binary alloy with equilibria as a function of composition and temperature. A particular pressure, typically 1 atm, is implicit but it is in principle possible to extend the diagram with a pressure axis.

As we will see in Chapter 4, the state assumed in equilibrium is the one that minimizes the free energy F . To construct a phase diagram, one thus needs to know the free energy as a function of composition and temperature. The situation becomes interesting once the free energy curve contains a convex region. The system can then decompose in two phases, the sum of which has a lower free energy than does the non-decomposed phase.

Consider an alloy with a free energy curve $F(c)$ such as the red one in Fig. 3.1(a). At concentration c_0 , the system has a free energy $F(c_0)$. If the system decomposes in two phases with concentrations c_1 and c_2 in proportions α_1 and α_2 , the new free energy is

$$F_{\text{decomposed}} = \alpha_1 F(c_1) + \alpha_2 F(c_2) \quad (3.1)$$

but the mass of either element needs to be conserved, so we require

$$\alpha_1 c_1 + \alpha_2 c_2 = c_0 \quad \text{and} \quad \alpha_1 + \alpha_2 = 1. \quad (3.2)$$

Combining the equations we find

$$\alpha_1 = \frac{c_2 - c_0}{c_2 - c_1} \quad \text{and} \quad \alpha_2 = \frac{c_1 - c_0}{c_2 - c_1} \quad (3.3)$$

and the new free energy becomes

$$F_{\text{decomposed}} = \frac{c_2 - c_0}{c_2 - c_1} F(c_1) + \frac{c_1 - c_0}{c_2 - c_1} F(c_2). \quad (3.4)$$

The question is then whether such a decomposition lowers the free energy (compared to $F(c_0)$) and which values of c_1 and c_2 minimize $F_{\text{decomposed}}$. It is a simple matter of differentiation and algebra to show that an extremum is reached for c_1 and c_2 chosen such that

$$\left. \frac{\partial F}{\partial c} \right|_{c=c_1} = \left. \frac{\partial F}{\partial c} \right|_{c=c_2} = \frac{F(c_2) - F(c_1)}{c_2 - c_1}, \quad (3.5)$$

which implies that the tangents at $F(c_1)$ and $F(c_2)$ coincide (dashed lines in Fig. 3.1(a)). This extremum is a minimum only if this tangent lies below $F(c_0)$. The family of such tangents that lie below $F(c)$ is referred to as the convex hull. The system decomposes in regions where the convex hull deviates from $F(c)$. Such regions are referred to as multi-phase regions and an alloy phase diagram is a map where the boundaries for these regions are drawn for each temperature [Fig. 3.1(b)].

3.2 Mean field treatment of the Ising model

The previous section discussed the emergence of two-phase regions for a material with a given free energy $F(c)$ but nothing was said about how this function emerges physically. The free energy (in this case the Helmholtz free energy) is defined as

$$F = U - TS \quad (3.6)$$

where U is the internal energy, T the temperature and S the entropy. The internal energy U depends on the binding energies between the atoms in the material. The entropy S , on the other hand, is oblivious to the chemistry of the components; it is only a function of how the atoms of type A and B are ordered in the lattice (vibrational entropy is neglected here).

The arguably simplest model of a binary alloy is the Ising model, in which the internal energy is written as a sum of interactions between nearest neighbors. This interaction

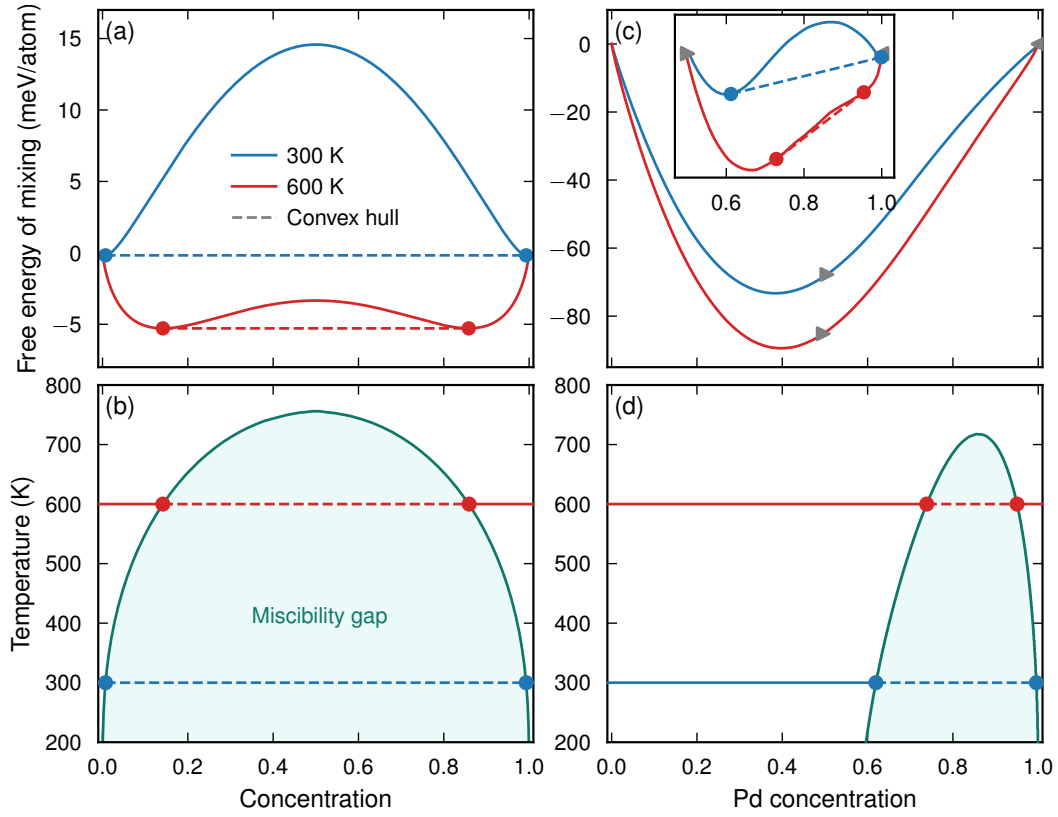


Figure 3.1: Construction of phase diagrams (b, d) from free energy curves (a, c) for two different models: the mean-field approximation of the Ising model Eq. (3.9) with $\omega = 0.13$ eV/atom (a, b) and Ag-Pd modeled with a cluster expansion and Monte Carlo simulations (c, d) [31]. The inset in (c) is a magnification of the Pd-rich side where a concave region appears.

may take one of two different values, u_0 if the nearest neighbors are alike or u_{A-B} if they are unlike. In an infinite crystal with completely random order (referred to as an ideal solution), each atom will on average have nc neighbors of type A and $n(1-c)$ neighbors of type B, where n is the number of nearest neighbors for each atom and c the overall concentration of A atoms. It is a simple algebraic exercise to show that the internal mixing energy¹ for the system can then be written

$$U_{\text{mix}}(c) = U(c) - cU(1) - (1-c)U(0) = N\omega c(1-c), \quad (3.7)$$

where N is the total number of atoms and $\omega = n(u_{A-B} - u_0)$. Furthermore, the config-

¹The mixing energy is often more convenient than the total energy for constructing phase diagrams for the sake of visualization, but the physics is the same.

entropial entropy in the completely random state is

$$S(c) = -Nk_B \sum_i p_i \ln p_i = -Nk_B [c \ln c + (1 - c) \ln(1 - c)] \quad (3.8)$$

because each site is occupied by an A or B atom with probability $p_A = c$ and $p_B = 1 - c$, respectively. Putting it all together, we have a free energy of mixing per atom

$$F_{\text{mix}}(c) = \omega c(1 - c) + k_B T [c \ln c + (1 - c) \ln(1 - c)]. \quad (3.9)$$

If the bond between unlike atoms is stronger than the bond between alike atoms, such that $\omega < 0$, then $F_{\text{mix}}(c)$ is negative and convex for all temperatures. If like atoms bind stronger than unlike, however, then the function will have a concave region at sufficiently low temperatures. As derived in the previous section, the system will then decompose – in other words, it has a miscibility gap. This situation is illustrated in Fig. 3.1(a–b) for two values of T along with the resulting phase diagram. The phase boundary for the miscibility gap (the *solvus* line) maps the maximum concentration at which B can dissolve in A or vice versa as a function of temperature. This limit is referred to as the solubility of either element in the other.

3.3 Order and disorder

In the mean field treatment of the Ising model we assumed random order and arrived at an expression with only one material-dependent parameter, ω . This is of course an oversimplification of a real material. In general, minimization of F leads to a competition between U and TS . If the interaction between unlike atoms is favorable enough, the material will be ordered such that the number of such bonds is larger than in the completely disordered state. An ordered phase has a lower entropy than a random one and will thus only be stable at low enough temperatures. Furthermore, the character of this order will depend on the details of the atomic interaction, for which the Ising model does not in general provide a sufficient description. Usually, however, a generalized Ising model (an alloy cluster expansion [32, 33]) can predict the correct phases, because they can usually be described with a small supercell of the primitive cell [34].

Ag–Pd is an example of a system where order plays an important role. Some ordered structures, in particular the $L1_1$ structure in which pure Ag and Pd planes are alternately stacked in the $\{111\}$ direction, have a substantially lower internal energy than randomly ordered structures. On the Pd-rich side of the free energy curve, however, there is a relative lack of such low-energy structures. The consequence is a concave region [Fig. 3.1(c)], which implies a two-phase region in the phase diagram [Fig. 3.1(d)]. This two-phase region is different from the one in the Ising model in the sense that it is caused by “too” favorable bonds between unlike atoms at some compositions, rather

than the unfavorable bonds of the Ising model with $\omega > 0$. This type of behavior is not unusual in metallic alloys, and ordered phases occurring in a narrow region in a phase diagram are sometimes referred to as intermetallic compounds.

It is in general difficult to predict the mixing behavior of two elements without sophisticated first-principles methods. A number of simple rules according to William Hume-Rothery [35] do, however, attempt a prediction of whether two elements form a substitutional solid solution:

- the atomic radii should differ by no more than 15 %,
- the crystal structures of the two elements should be similar,
- the two elements should have the same valency, and
- the two elements should have similar electronegativity (if they differ too much, an intermetallic compound is likely to form).

The predictive power of these rules is limited if applied blindly, but they identify a number of parameters that may have influence. It is thus tempting to attribute the low solubility of Ag in Cu and vice versa to their 19 % difference in size [36], and the tendency of Au–Cu to form intermetallic compounds to their 34 % difference in electronegativity [37, 38], and although such explanations of material properties are likely to be oversimplified and incomplete, they certainly provide a more tangible picture than a set of full many-body wave functions.

3.4 Chemical order in nanoalloys

The different possible orderings in macroscopic alloys pervade nanoalloys as well; the mixing behavior in the bulk alloy is usually expected to be similar in the corresponding nanoalloy. The existence of a surface, a finite number of atoms, strain and possibly polycrystallinity as in a decahedron or icosahedron do, however, allow for new behavior and modification of the ranges at which particular phases are stable. This has been demonstrated in computationally assessed phase diagrams for a wide range of nanoalloys, including Pt–Rh [39], Ag–Au [40], Au–Cu [41], several Ni-based alloys [42], and an artificial Lennard-Jones alloy [43]. It has also recently become possible to experimentally image the chemical order of nanoalloys atom by atom using atomic electron tomography [44]. Where models on the atomic scale would previously be compared indirectly to observations in the laboratory, there is now an exciting avenue to a level playground between theory and experiment.

A long-standing debate is whether or not miscibility is increased at the nanoscale. This chapter has ignored that phase separation comes with a cost; the interface between two phases is associated with a free energy penalty $A\gamma$, where A is the area of

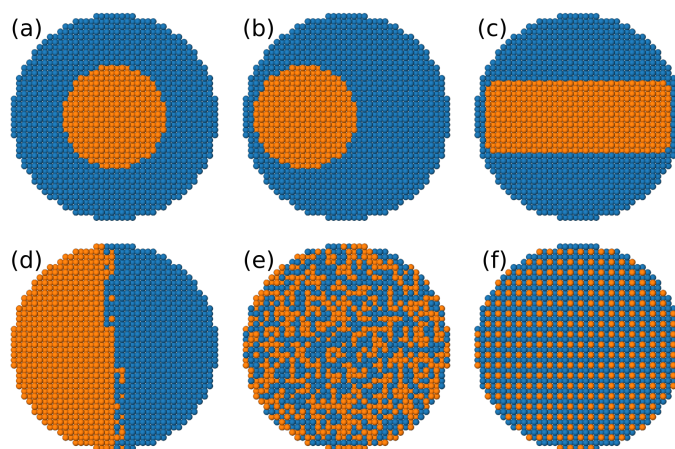


Figure 3.2: Nanoalloys with idealized chemical orderings: (a) core–shell, (b) off-center core–shell, (c) sandwich, (d) Janus, (e) random and (d) ordered.

the interface and γ an interface energy dependent on the phases, the orientation of the interface etc. In a bulk system, this term can be ignored because one can assume the interface area to be small compared to the volume of the system. In a nanoalloy, however, this assumption may break down. An initial analysis of the consequences may be carried out by adding the $A\gamma$ -term to Eq. (3.4) [45],

$$F_{\text{decomposed}} = \frac{c_0 - c_2}{c_1 - c_2} F(c_1) + \frac{c_1 - c_0}{c_2 - c_1} F(c_2) + A\gamma. \quad (3.10)$$

For a nanoparticle with radius r , the first two terms scale with r^3 whereas the last term scales with r^2 and one would thus expect that there is a critical radius below which phase separation does not occur. Some experimental studies have supported this supposition [46, 47, 48, 49, 50, 51], in particular for Au–Pt nanoalloys, but conclusions from some of these studies have been questioned [52] and one should remember that it is difficult to know whether thermodynamic equilibrium has been reached. There have been very few signs of increased miscibility in computational studies [53, 43]. In one of the most recent contributions to the debate [54], the absence of increased miscibility was explained with the existence of special sites in nanoparticles; unlike a bulk system, a nanoparticle has many symmetrically distinct sites on which the atoms may order such that the interface does not increase the total free energy. Paper II essentially supports this conclusion for the Ag–Cu system. In fact, it was observed that because of the underlying nanoparticle structure, the interface in equilibrium is much larger than it needs to be geometrically, but the system is still clearly phase separated.

While the debate on equilibrium chemical ordering continues, experimentalists keep synthesizing nanoalloys that are not in equilibrium, often with a particular application in mind. Some nomenclature has emerged to systematize possible structures (Fig. 3.2).

The core–shell structure [Fig. 3.2(a)] is particularly ubiquitous, partly because it is possible to synthesize for a wide range of alloys, including alloys that would mix in thermodynamic equilibrium. A core–shell structure can for example be of economic interest for an application where the element at the surface of the particle is important but expensive and can be filled with a cheaper element in the core. Computational studies show that the core is often asymmetrically positioned in equilibrium [Fig. 3.2(b)]. The investigation of Ag–Cu in Paper II further indicates that the notion of a core is in some structures merely a special case for a more complex segregation pattern, which at some compositions may lead to a ring-like sandwich pattern [Fig. 3.2(c)]. The shape of the segregate is thus largely dictated by the underlying structure of the particle. So-called Janus particles, where the elements segregate at either side of the particle [Fig. 3.2(d)], are attractive for some applications primarily because they are inherently anisotropic. Randomly mixed nanoalloys [Fig. 3.2(e)] and nanoalloys with long-range order [Fig. 3.2(e)] are often desirable for applications in catalysis, where there can be a synergistic effect from the two elements. There are of course many more possibilities than the highly idealized structures described here, and some of them are illustrated in Paper II.

Statistical mechanics at the bulk and nanoscale

Ordinary thermodynamics is strictly valid only in the thermodynamic limit where the number of particles tend to infinity or is at least on the order of 10^{23} or so [55]. Take, for example, the expression for the energy of a nanoparticle introduced in Chapter 2 [Eq. (2.1)]. The internal energy is an extensive property in ordinary thermodynamics – if we double the number of atoms, the energy doubles as well. This is clearly not the case in the nanoparticle energy expression. This violation invalidates many of the expressions that we know from thermodynamics and a more careful treatment is called for. The generalization to smaller systems is not entirely straight-forward, and even though frameworks have been laid out [56], several subtle aspects are still subject to debate [57, 58, 59]. This thesis does not attempt to navigate this minefield but resorts to statistical mechanics, which is equally valid in small and large systems. Yet, as in the previous chapter, a thermodynamic terminology is often used but should sometimes be understood in an approximate sense. This chapter uses statistical mechanics to highlight a few aspects where macroscopic and nanoscale systems differ.

4.1 Statistical mechanics in the thermodynamic limit

Consider a system in contact with a heat reservoir. All information about the system is encoded in its partition function,

$$Z = \sum_s e^{-\epsilon_s/k_B T}. \quad (4.1)$$

Here, the sum is taken over all microstates s with corresponding energy ϵ_s . It is common (but often implicit) practice in statistical mechanics to coarse-grain the system. We may for example group all microstates that have the same energy E ,

$$\begin{aligned} Z &= \sum_E \sum_{s \rightarrow E} e^{-\epsilon_s/k_B T} = \sum_E \Omega(E, V, N) e^{-E/k_B T} \\ &= \sum_E \exp \left[(k_B T \ln \Omega(E, V, N) - E) / k_B T \right]. \end{aligned} \quad (4.2)$$

The quantity $\Omega(E, V, N)$ counts the multiplicity of each macrostate N, V, E , i.e., how many microstates that correspond to energy E (at this particular volume V and number of particles N). Ludwig Boltzmann used this quantity to define entropy, $S(E, V, N) = k_B \ln \Omega(E, V, N)$, so we may write our partition function as

$$Z = \sum_E \exp \left[-(E - TS(E, V, N)) / k_B T \right]. \quad (4.3)$$

We know from ordinary thermodynamics of macroscopic systems that TS and E are usually on the order of kilojoules, whereas $k_B T$ at room temperature is on the order of tens of millielectronvolts. The exponents are thus on the order of 10^{23} , which makes the terms of Eq. (4.3) unfathomably large. Any term in which the exponent is just a tiny fraction larger than the others will completely dominate the sum. It is thus of great interest to study the quantity in the exponent. We refer to it as free energy, in the case of the canonical partition function the Helmholtz free energy;

$$F = E - TS(E, V, N). \quad (4.4)$$

Whichever energy E minimizes F will completely dominate the partition function, and will thus be an overwhelmingly more likely macrostate to observe than any other. We can thus write

$$Z \approx e^{-F_{\min}/k_B T}. \quad (4.5)$$

So while Eq. (4.4) indicates a dependency on energy E , one would usually write (or rather mean)

$$F(T, V, N) = F_{\min} = \langle E \rangle - TS(\langle E \rangle, V, N), \quad (4.6)$$

which indicates that the minimization has already been carried out and that Eq. (4.4) has been evaluated at the minimizing energy, $\langle E \rangle$. We may conclude that probability favors a particular state with a particular energy E and we refer to this as the equilibrium state.

4.2 Small systems

In the previous section, we assumed a macroscopic system ($N \approx 10^{23}$). For nanoparticles in which the number of atoms is on the order of 10 to 10^8 , some of the conclusions

are not valid and one has to tread carefully. One important consequence is that fluctuations of macroscopic quantities, which vanish in the thermodynamic limit, can become appreciable in small systems. Consider, for example, the variance in energy in the canonical ensemble (using $\beta = 1/k_B T$),

$$\text{Var}E = \langle E^2 \rangle - \langle E \rangle^2 = \frac{1}{Z} \sum_E E^2 e^{-\beta E} - \left(\frac{1}{Z} \sum_E E e^{-\beta E} \right)^2 \quad (4.7)$$

$$= \frac{1}{Z} \frac{\partial^2 Z}{\partial \beta^2} - \frac{1}{Z^2} \left(\frac{\partial Z}{\partial \beta} \right)^2 = \frac{\partial}{\partial \beta} \left(\frac{1}{Z} \frac{\partial Z}{\partial \beta} \right) = -\frac{\partial \langle E \rangle}{\partial \beta} = \quad (4.8)$$

$$= k_B T^2 \frac{\partial \langle E \rangle}{\partial T} = k_B T^2 C \quad (4.9)$$

where C is the heat capacity. Assuming that $\langle E \rangle$ and C scale with the number of particles (which would be an approximation for a small system), we have that the relative fluctuations scale as

$$\frac{\sqrt{\text{Var}E}}{\langle E \rangle} = \frac{\sqrt{k_B T^2 C}}{\langle E \rangle} \propto \frac{1}{\sqrt{N}}. \quad (4.10)$$

Fluctuations are thus negligible in large systems but can be comparably large in small systems. As an illustration, we may take a metal nanoparticle with 1000 atoms. The heat capacity of a metal at sufficiently high temperature is usually approximated well by $C \approx 3Nk_B$ so that the (absolute) fluctuations at room temperature ($k_B T \approx 25$ meV) are on the order of $\sqrt{3 \times 1000 \times (25 \text{ meV})^2} \approx 1$ eV or 1 meV/atom. Although this value may appear small, the results of Paper I show that it is of the same magnitude as the difference between the energies of structural motifs, which indicates that thermal fluctuations may be sufficient to cause structural transitions in nanoparticles unless energy barriers are too high.

Another difference between large and small systems is that the ensembles are equivalent in the former but not necessarily in the latter [60]. This means that it does not matter whether a macroscopic system is isolated or in contact with a heat bath as long as the average energy of the thermostated system is the same as the one in the isolated system – any measured quantity will have the same value in the two systems. This need not be true in a microscopic system.

Furthermore, phase transitions are smoothed below the thermodynamic limit, essentially a consequence of a finite number of terms in the partition function. In addition to a smooth behavior, it has been observed that the transition temperature and the associated latent heat tend to be lowered in small systems [60, 61].

Although large and small systems differ in several aspects, it should be stressed that the fundamental assumptions of statistical mechanics, for example that the probability of a state in the canonical ensemble is $e^{-\beta e}/Z$, are the same regardless of system size.

The differences lie merely in the consequences, meaning that some calculations may become more laborious or that results from the thermodynamic limit have to be taken as approximations in finite systems. This thesis, in which nanoparticles with more than a few hundred atoms are the protagonists, has the approximations approach as its philosophy.

4.3 Ensembles of nanoparticles

Statistical mechanics has as one of its key components ensembles, i.e., large sets of virtual copies of the system in different states. This concept indeed appears somewhat virtual in the thermodynamic limit where there is usually only one real system. For nanoparticles, on the other hand, “ensembles” are realized in real systems all the time; a laboratory making one nanoparticle at a time would hardly make a profitable business. A dilute solution of nanoparticles is for example well approximated by a canonical ensemble for which the solvent is the heat reservoir. Unlike the virtual copies of a statistical mechanics ensemble, the nanoparticles in such a system do interact by heat exchange with the solvent, but if the solvent is voluminous enough to have an essentially infinite heat capacity, this interaction is merely indirect. A seemingly trivial but delightful consequence is that if we calculate, say, that the probability in the canonical ensemble for a certain nanoparticle to be an icosahedron is 30 %, a solution with 10,000 such particles should have on average 3,000 icosahedra.

In a similar fashion, we can imagine a solution of nanoparticles that may exchange both energy and atoms with the solvent. Even though atoms would be exchanged between particles, each particle may be considered an independent system interacting with a reservoir of heat and single atoms. The corresponding ensemble is referred to as grand canonical, and the probability for a particular state for a single particle is calculated as

$$\mathcal{P}(s) = \frac{e^{-\beta(\epsilon_s - \mu N)}}{\mathcal{Z}}, \quad (4.11)$$

where μ is the chemical potential of the atoms that are being supplied from the solution, N is the number of atoms in the particle and \mathcal{Z} is the partition function in the grand canonical ensemble (a sum over all states of terms such as the one in the numerator).

In practice, an equilibrium solution of metallic nanoparticles that exchange atoms with the solution may be difficult to realize in an experiment, because the atoms are generally much too strongly bound to be released to the solution. The experimental problem is rather the opposite, that nanoparticles tend to cluster into bigger entities, a phenomenon usually prevented by stabilizing organic molecules on the surface of the particles. The atom count for each particle is to a large extent established during growth, when the particles assemble atoms from a solution of a metal salt and a reducing agent. This process is predominantly kinetically driven and can usually only

be understood partially from an equilibrium perspective. The result is always that the particle ensemble is more or less polydisperse, i.e., the particles have different numbers of atoms, but the size distribution is, as a manifestation of the central limit theorem, usually well described by a normal distribution regardless of synthesis route.

If the properties of nanoparticles were smooth functions of atom count, a polydisperse ensemble would show similar properties as a monodisperse one. But this may not always be the case, because as mentioned in Sect. 2.5, nanoparticles tend to exhibit magic numbers for which particles are perfectly symmetric in some structural motifs. The density of magic numbers is different for different structural motifs, and in Paper I we demonstrate that there are also “semi-magic” numbers for which the outermost atomic shell has covered some facets but not others. This possibility points to the importance of considering the whole distribution of sizes in a polydisperse ensemble and not just the average size. In Paper I, we assumed a normal distribution $f(n, N)$ of atom counts n with average atom count N . For each atom count, we then assumed a Boltzmann distribution of shapes, such that the probability of a shape s_0 is

$$\mathcal{P}_n(s_0) = \frac{\exp(-\beta\epsilon_{n,s_0})}{\sum_{s_i} \exp(-\beta\epsilon_{n,s_i})}, \quad (4.12)$$

where ϵ_{n,s_i} is the lowest energy of any particle with n atoms in structural motif s_i . The probability for a particular shape for an ensemble with average size N was then calculated as

$$\mathcal{P}_N(s_0) = \frac{1}{M} \sum_n f(n, N) \mathcal{P}_n(s_0) \quad (4.13)$$

where M ensures that the probabilities sum up to 1. Fed with the results from the algorithm of Paper I, this model indicates that there is a distribution of structural motifs in thermodynamic equilibrium. The model assumes that energetics does not affect the distribution of atom counts; it is not more probable to have a particle with 923 atoms just because it is an icosahedral magic number. This may or may not be a valid assumption, depending on the growth protocol. It is perhaps more questionable that only the ground states for three structural motifs were taken into account, and all with the same multiplicity. Whereas inclusion of more structural motifs with higher energy could only strengthen the conclusion that there is a distribution of shapes in thermodynamic equilibrium, it cannot be ruled out that an account for multiplicity could have the opposite effect. Furthermore, elevated temperatures, which are assumed in the Boltzmann factors of Eq. (4.12), may favor some structural motifs over the others, primarily due to vibrations. This has been demonstrated in the case of Au, for which decahedral particles were seen to be stabilized by temperature relative to the other structural motifs [28].

Computational methods

The overarching theme of this thesis is the prediction of nanoparticle characteristics on the atomic scale. To this end, an essential ingredient is the calculation of potential energy as a function of atomic positions. The Schrödinger equation provides a solid fundamental basis, which in theory provides a sufficient description on which we could base our calculations. The problem, however, is one of scales; we want to address systems with thousands of atoms, meaning tens of thousands of electrons, and we need to calculate the energy of these systems millions of times to evaluate partition functions and identify ground states. Not even the most efficient techniques and approximations in quantum mechanical calculations are sufficient to tackle this problem. The situation calls for a much more efficient approach, and a viable option is provided by interatomic potentials and molecular dynamics (MD). The resulting framework is purely classical mechanics. This chapter describes and motivates the use of these methods, along with a few other computational techniques of relevance in the thesis.

5.1 The Born–Oppenheimer approximation

Why is a classical mechanics approach to an atomic scale problem valid? The physics and chemistry of a material are largely governed by its electronic structure, and electrons at room temperature have a de Broglie wavelength of more than 4 nm, which is much longer than the interelectronic distances, and thus much too long for a classical description to be valid. The resolution is the application of the Born–Oppenheimer approximation, which formalizes the consequences of the difference in mass between the atomic nuclei and the electrons. In this approximation, the wave function is assumed to be separable in an electronic and an ionic part, and the electrons are assumed to instantaneously assume the ground state for given positions \mathbf{r} of the ions. The result is that

the Schrödinger equation for the full system can be simplified to a Schrödinger equation for the ionic wave function only, but with an effective potential $U(\mathbf{r})$ incorporating the energy of the electrons [62],

$$U(\mathbf{r}) = U_{ZZ}(\mathbf{r}) + \epsilon_0(\mathbf{r}). \quad (5.1)$$

Here, $U_{ZZ}(\mathbf{r})$ is the potential energy from ion-ion interaction and $\epsilon_0(\mathbf{r})$ the ground state energy of the electrons with ions fixed in positions \mathbf{r} . The de Broglie wavelength of an atomic nucleus in room temperature is always much smaller than the interatomic spacing, in particular for the heavier elements. A classical treatment of the ions is thus warranted, and since $U(\mathbf{r})$ is the effective potential for the ions, we can use it in the same way as we would use any classical potential. The quantum mechanics of the electrons is then implicitly taken into account in the functional form of $\epsilon_0(\mathbf{r})$. It is worth noting that even though $U(\mathbf{r})$ is often referred to as the potential energy of the atoms, it contains also the kinetic energy of the electrons via $\epsilon_0(\mathbf{r})$.

5.2 Interatomic potentials

The possibility to use a classical potential to describe the energetics of a material is a blessing only if we can find a proper form for the interatomic potential $U(\mathbf{r})$. Whereas an exact expression is of course unattainable, many attempts have been made to find proper functional forms that can be fitted to experimental observations or theoretical results from quantum mechanics (usually obtained with density functional theory (DFT) calculations). Some of the first attempts can be classified as pair potentials, which are simply sums over pairs of atoms,

$$U(\mathbf{r}) = \frac{1}{2} \sum_{\substack{i,j \\ i \neq j}} \phi_{ij}(r^{ij}). \quad (5.2)$$

Here, r^{ij} denotes the distance between atom i and j . The remaining task is to determine the form of ϕ , which, however, is a one-dimensional function and thus tractable to parametrize empirically. Examples of pair potentials include the forms suggested by Lennard-Jones and Morse already in the 1920s.

5.2.1 Embedded atom method

Pair potentials have merit in their simplicity but fail to reproduce fundamental properties of most materials. A deficiency particularly damaging for metals is the built-in dependency of energy on the number of bonds in pair potentials. This bond-counting nature forces the energy to scale linearly with the coordination number (the number of

neighbors for a given atom). In a real metal, on the other hand, the energy scales more closely with the square root of the coordination number; a bond formed in isolation is stronger than a bond formed in presence of other bonds [62, 63].

The expected scaling can be reproduced by introducing a second term,

$$U(\mathbf{r}) = \frac{1}{2} \sum_{\substack{i,j \\ i \neq j}} \phi_{ij}(r^{ij}) + \sum_i F_i(\rho^i). \quad (5.3)$$

Here, F is a functional dependent on a yet unspecified function ρ . A number of potentials of this or similar forms were published in the 1980s and have come to be known as embedded atom method (EAM) [64], effective medium theory [65, 66], Finnis–Sinclair potentials [67], glue potentials [68] etc. The nomenclature is more diverse than the physics, and we will base the discussion on EAM, which is employed in Papers I and II.

In EAM potentials, the functional F_i is referred to as the embedding term and depends on a linear superposition of the electron densities from the neighboring atoms [63],

$$\rho^i = \sum_{j \neq i} \rho_j^a(r^{ij}). \quad (5.4)$$

Here, ρ^a is a function that remains to be determined and just as before, r^{ij} is simply the distance between atom i and j , meaning that the electron density from each atom is approximated as spherically symmetric. Such a superposition of electron densities can be motivated by the Hohenberg–Kohn theorems [69], from which it is known that the energy can be written as a functional of the electron density. This concept was further elaborated by Stott and Zaremba [70] who showed that the energy of an impurity embedded in a host is a functional of the electron density of the unperturbed host. The impurity may in this case simply be the same kind of atom as the host. This shows that there is a fundamental reason for writing the energy as a functional of the electron density of the neighboring atoms, even though the exact form of this functional is unknown.

To construct an EAM potential for a specific material, one needs to determine ϕ , F and ρ^a . This is typically done by choosing certain physically reasonable functional forms with the desired number of free parameters and fitting those parameters to experimental and/or first-principles data for certain materials properties, which may include cohesive energy, lattice parameter, elastic constants, thermal expansion coefficients, defect formation and migration energies, phonon frequencies etc, all in one or more crystal structures. This task needs to be carried out with care and all potentials have a limited range of applicability, largely determined by the input data in the parameter fit.

As we have seen, EAM potentials assume a spherically symmetric electron density centered at each atom. Their accuracy is thus dependent on a high degree of non-

directional bonding. The late transition metals are particularly well suited in this regard, because their filled d band (and s orbital in the case of the coinage metals) gives rise to a predominantly spherically symmetric electronic structure and thus low degree of directionality. For materials with a high degree of directionality, most notably covalently bonded solids such as diamond and silicon, other functional forms are needed and a viable approach is to include three-body terms, which is, however, beyond the scope of this thesis in which all closely studied materials are late transition metals.

5.3 Atomistic simulations

An interatomic potential is an extremely efficient tool for calculating energies and forces in atomistic systems. With such a tool, one can efficiently sample a large number of states and thus calculate a wealth of materials properties.

5.3.1 Molecular dynamics

One of the most obvious application of interatomic potentials is to temporally evolve a system of atoms in some geometry according to Newtonian mechanics. This has been coined molecular dynamics (MD). Every atom i in a MD simulation is assigned an initial coordinate \mathbf{r}_i and momentum \mathbf{p}_i and the system is propagated in time with each atom acting on every other according to Newton's second law,

$$\mathbf{F}_i = -\nabla U(\mathbf{r}_i) = \ddot{\mathbf{p}}_i. \quad (5.5)$$

The basic idea is simple but the actual implementation may be complicated with a wealth of considerations regarding, for example, discretization of time and space, boundary conditions, cutoffs in the interatomic potential and baro- or thermostats to mimic a desired physical situation.

5.3.2 Time and ensemble averages

Physical quantities are usually extracted from MD simulations by taking averages over time,

$$\bar{f} = \frac{1}{\tau} \int_0^\tau f(t) dt. \quad (5.6)$$

Here, f is the sought-for physical quantity, t time and τ a certain time interval. The spirit is the same as an experimental measurement, which does also always occur over some time, short or long. It is often assumed that the time average equals the ensemble average,

$$\langle f \rangle = \frac{\int f(\mathbf{r}, \mathbf{p}) e^{-\epsilon(\mathbf{r}, \mathbf{p})/k_B T} d\mathbf{r}^N d\mathbf{p}^N}{\int e^{-\epsilon(\mathbf{r}, \mathbf{p})/k_B T} d\mathbf{r}^N d\mathbf{p}^N}. \quad (5.7)$$

If the ergodic hypothesis holds for the system at hand, i.e., all microstates are equally probable over a sufficiently long time scale, we may indeed have $\bar{f} = \langle f \rangle$. In this context, it needs to be stressed that atomic motion occurs on the scale of picoseconds, which means that a typical MD simulation rarely exceeds microseconds and typically much less. The risk of having a system trapped between energy barriers in a certain part of phase space over the time scale of the simulation is thus significant, such that the time average will differ from the ensemble average even if the ergodic hypothesis holds for the system under consideration. A good example is a metallic alloy, for which atoms rarely exchange sites, hindering the use of MD for sampling configuration space. In such systems, other computational methods are called for.

5.3.3 Monte Carlo simulations

Monte Carlo (MC) represents a wide class of computational methods that rely on sampling with a component of randomness to evaluate multidimensional integrals. Here, Monte Carlo (MC) will be described in a limited scope as applied to configurational sampling of an alloy using the Metropolis algorithm. In such a simulation, the atoms are fixed and the system is described by the chemical identity of the atoms on each site. The simulation consists of changing the chemical identities on trial, and accepting or rejecting the change based on a carefully chosen criterion. Metropolis *et al.* [71] chose the criterion

$$\mathcal{P}(\text{accept}) = \min \{ 1, \exp(\Delta E/k_B T) \} \quad (5.8)$$

where ΔE is the change in potential energy caused by the trial. This choice ensures that an ensemble of systems subject to this criterion approaches the canonical ensemble [71], or in other words, a single simulation will sample a Boltzmann distribution. In the canonical ensemble, the concentration is always conserved, which means a trial change will always consist of a swap of chemical identity between two sites with unlike atoms. Such MC simulations may overcome the inability of MD to properly sample all of configuration space, because the simulation knows fewer energy barriers; all calculated quantities are ensemble averages and the algorithm is usually not designed as to simulate a real trajectory.

5.3.4 The semi-grand canonical ensemble

The Metropolis criterion is readily generalized to ensembles other than the canonical. The procedure is to simply switch ΔE in Eq. (5.8) to the change in the thermodynamic potential associated with the ensemble to be sampled (excluding the $-TS$ term). For alloys, a common choice is the semi-grand canonical (SGC) ensemble. This ensemble corresponds to a physical situation in which the difference in chemical potential between different species is fixed (in addition to temperature, volume and total number

of atoms N). The SGC ensemble thus allows the concentrations to fluctuate, such that a trial change can be taken as the change of chemical identity on a single site, i.e., no swap of two sites as in the canonical ensemble. A Legendre transformation [55] reveals that the thermodynamic potential associated with the ensemble is

$$\psi = E + Nc\Delta\mu - TS, \quad (5.9)$$

where N is the total number of atoms, $c = N_A/N$ the concentration of species A , and $\Delta\mu = \mu_A - \mu_B$ the difference in chemical potential between species A and B . The modified Metropolis criterion is thus

$$\mathcal{P}(\text{accept}) = \min \left\{ 1, \exp \left[(\Delta E + N\Delta c\Delta\mu) / k_B T \right] \right\}. \quad (5.10)$$

In MC simulations of alloys, the SGC ensemble has at least two advantages over the canonical ensemble. Firstly, the acceptance probability may get very low when using the canonical ensemble for a system where moves that keep the energy low are rare. The probability of lowering the energy when swapping two randomly picked sites, as is done in the canonical ensemble, is essentially the square of the already low probability of finding a favorable switch. Secondly, the allowance to vary concentration makes it simple to continuously carry the system from one composition to another and integrate the free energy along the path. The theoretical foundation for the free energy integration is derived in a fashion similar to Sect. 4.1. The SGC partition function \mathcal{Z} can be coarse-grained in energy and concentration,

$$\begin{aligned} \mathcal{Z} &= \sum_s \exp \left[-(\epsilon_s + Nc\Delta\mu) / k_B T \right] \\ &= \sum_{c,E} \Omega(c, E) \exp \left[-(E(c) + Nc\Delta\mu) / k_B T \right] \\ &= \sum_{c,E} \exp \left[-(E - TS(E, V, N, c) + Nc\Delta\mu) / k_B T \right] \\ &\approx \sum_c \exp \left[-(F(T, V, N, c) + Nc\Delta\mu) / k_B T \right]. \end{aligned} \quad (5.11)$$

The last step introduced the canonical free energy $F(T, V, N, c)$ in the same fashion as in Sect. 4.1 and with emphasis on the fact that it is defined as a function of concentration c . For every value of T , N and $\Delta\mu$, and for a sufficiently large system, the term with the largest exponent will dominate the sum. Assuming the exponent is differentiable in c , we have

$$\frac{\partial}{\partial c} (F(T, V, N, c) + Nc\Delta\mu) = 0 \quad (5.12)$$

so that

$$\frac{\partial F}{\partial c} = -N\Delta\mu. \quad (5.13)$$

In practice, the canonical free energy can thus be recovered from a MC simulation in the SGC ensemble by continuously varying $\Delta\mu$ and recording the average concentration. It is worth noting that the thus calculated free energy is not the one that is formally minimized in the SGC ensemble, but the derivation is anyway strictly valid only for large systems in which the ensembles are equivalent and this issue has no practical consequences.

The SGC ensemble is, however, limited in systems with multi-phase regions, because $\Delta\mu$ maps to multiple values of the concentration in such regions. A MC simulation in the SGC ensemble will not be able to stabilize in such a region, but will discontinuously jump between the phase boundaries. While such jumps contain information that may be exploited to, for example, construct phase diagrams, they prevent extraction of information from within the multi-phase region.

5.3.5 The variance-constrained semi-grand canonical ensemble

To overcome the limitations of the SGC ensemble in multi-phase regions, Sadigh *et al.* [72, 73] developed the variance-constrained semi-grand canonical (VCSGC) ensemble, which takes inspiration from the SGC ensemble but introduces a parameter $\bar{\kappa}$ that constrains the fluctuations (variance) of the concentration. Its thermodynamic potential can be written

$$\psi_V = E + \bar{\kappa} N k_B T (c + \bar{\phi}/2)^2 - TS \quad (5.14)$$

where $\bar{\phi}$ replaces $\Delta\mu$ as the parameter that drives the concentration. For a sufficiently large value of $\bar{\kappa}$, the mapping between $\bar{\phi}$ and c becomes single-valued so that a simulation can stabilize concentrations also inside multi-phase regions. A derivative of the canonical free energy can be derived in the exact same way as for the SGC ensemble, and one finds that

$$\frac{\partial F}{\partial c} = -2\bar{\kappa} N k_B T (c + \bar{\phi}/2). \quad (5.15)$$

It is thus possible to integrate the free energy across multi-phase regions by recording the average concentration in a MC simulation in the VCSGC ensemble.

5.3.6 Hybrid MD–MC simulations

When discussing the energetics of alloys, it is often convenient to split the partition function in a configurational and a vibrational part,

$$Z = \sum_{\sigma} \int_{\Omega_{\sigma}} e^{-E/k_B T} dr^N dp^N. \quad (5.16)$$

Here, the configurational part is represented by a sum over all possible decorations σ of the lattice, whereas the vibrational part is represented by a multidimensional integral

over the part of phase space Ω_σ consistent with each decoration. It is often advantageous to evaluate the different parts with different methods; because MD is particularly well suited for sampling the vibrational and MC the configurational part, we may combine the two. In practice, this means that we run a MD simulation but interrupt it at regular intervals to carry out a series of MC trial steps. A quantity of interest is then calculated by time averages over the vibrational part combined with ensemble averages over the configurational part. This technique was employed in Paper II.

5.4 Energy minimization techniques

MD and MC simulations are often used to study materials at a specific temperature. A well-behaved system will approach equilibrium, and equilibrium properties can be extracted by calculating averages and analyzing trajectories. As a special case, one is often interested in the equilibrium at zero temperature, i.e., the ground state. The ground state is conveniently characterized by a minimum in potential energy and is as such, if nothing else, attractively well-defined and of fundamental interest. For many systems it also often provides a reasonable approximation to the equilibrium state at room temperature, provided that the melting temperature is much higher. Unfortunately, it is not straightforward to extract the ground state from MD or MC simulations, because sampling can become prohibitively inefficient at low temperatures.

5.4.1 Spatial and configurational global optimization

The separation of the partition function in a configurational and a spatial part (as in Eq. (5.16)) is fruitful when facing the task of finding ground states in metallic systems. For monometallic particles, the configurational part disappears and the problem is essentially to position a given number of atoms in space such that their interaction yields the lowest energy. Given that every atom has three coordinates, this problem is extraordinarily difficult already for clusters with less than a few tens of atoms. The problem has received considerable attention and become the target of many novel optimization schemes [74]. A wide array of techniques exist [75, 76], many of which are based on either genetic algorithms [77, 78] or basin hopping [79, 80, 81].

The problem of optimizing the configuration, i.e., assigning an optimal ordering of chemical identities, is quite different, because in this case the possible states are discrete. For a binary system with N atoms of which N_A are of type A and N_B of type B , the number of possible configurations n is exactly

$$n = \frac{N!}{N_A!N_B!}. \quad (5.17)$$

Many of these are usually equivalent by symmetry, but the number is still extremely large for a few tens of atoms and non-dilute concentrations. This problem is even more

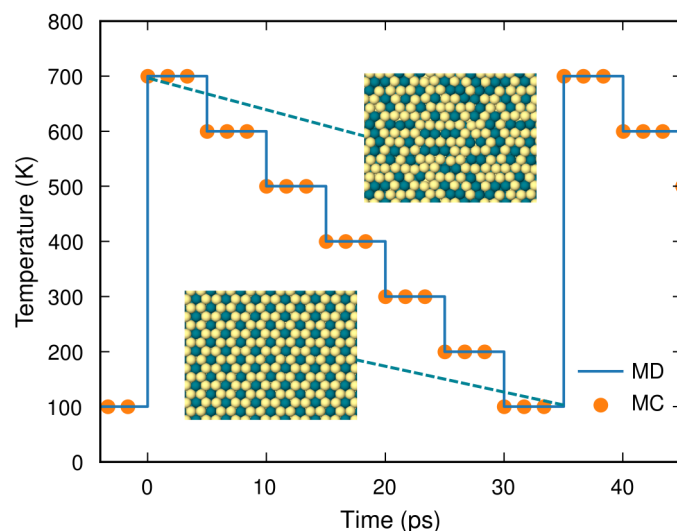


Figure 5.1: Schematic of simulated annealing in a hybrid MD–MC simulation, in this case for a Au–Pd {111} surface alloy. Orange dots indicate that the MD propagation is interrupted for MC trial steps. At high temperatures, the surface is disordered but as low temperatures are reached, the surface assumes an ordered ground state, in this case a honeycomb pattern.

well-studied than monoelemental optimization, but the gallery of useful optimization techniques turns out almost the same [75, 76, 82, 83, 84, 85], even though the possibility of lattice-based energy models for alloys opens an avenue to more specialized methods [86]. It should be stressed that the configurational and spatial parts are dependent; the optimal configuration may change as the positions of the atoms are changed. Global optimization of a nanoalloy is thus significantly more difficult than global optimization of a monoelemental particle.

5.4.2 Local optimization

The difficulty of the global optimization problem has necessitated restricted searches for local minima. A particularly common approach has been to restrict the positions of the atoms to the vicinity of a structural motif and then optimize the chemical configuration subject to that structure, possibly allowing local relaxation [87, 88, 89]. The structures have usually been chosen from the high-symmetry motifs described in Chapter 2. Both global minimizations and experimental observations have repeatedly pointed to the relevance of these structures, and even if a particular configuration in the chosen structure is not a global minimum, experimentally a nanoalloy may very well be kinetically trapped in that structure. This is the philosophy of Paper II.

5.4.3 Simulated annealing

Another widespread approach to optimization is simulated annealing (Fig. 5.1). It is inspired by the procedure an experimentalist might follow to quench a real system into its ground state. A MD or MC simulation is started at high temperature, where chances are good that energy barriers can be overcome, and the temperature is gradually lowered. The system is then expected to approach its ground state or a local minimum if the setup constrains the system to a certain part of phase space. There is a risk that the system is quenched into a funnel of the potential energy surface whose bottom is not the ground state. Still, simulated annealing does in practice often identify the global ground state, in particular if the process is repeated multiple times. Simulated annealing with hybrid MD–MC was employed in both Paper I and II.

5.5 Elastic strain

Elastic strain, being a measure of the deformation of a solid body, is in general described with a two-dimensional tensor with six independent components [90]. In this thesis, the term is usually used in a restricted sense referring to volumetric strain, i.e., the relative change in volume ($\Delta V/V$). Mathematically, the volumetric strain is the sum of the diagonal components of the strain tensor.

In the present context, the strain needs to be calculated on a per atom basis. This was done using the OVITO software [91] in both Paper I and II. The calculation relies on a comparison between the environment for each atom and the ideal crystal structure, here taken as the FCC structure with the bulk equilibrium lattice parameter. This comparison is only possible if the local structure is sufficiently similar to the ideal crystal structure, and is dependent on computational crystal structure identification [92]. As a consequence, atoms at interfaces (including twin boundaries and the surface of the particles), were excluded from the strain analyses.

Summary of the papers

6.1 Paper I

Paper I introduces an algorithm for predicting nanoparticle structures in a wide size range. At its core, it is a straight-forward application of MC simulations to the binary metal–vacancy system. This system is an extreme example of an immiscible system for which the SGC ensemble fails to stabilize any composition but pure vacuum and compact bulk. It thus provides an attractive use case for the VCSGC ensemble.

The algorithm is based on simulated annealing coupled to a sequential sweep of the concentration driving parameter ϕ of the VCSGC ensemble. MC trial steps changing atoms to vacancies or vice versa are regularly interrupted for atomic relaxation and the lowest energy structure for each number of atoms is recorded. The algorithm relies on an *a priori* definition of a structural “lattice”. In the paper, we chose the most well-studied ones, specifically single crystalline, decahedral, and icosahedral structural motifs. Atoms are only allowed to relax locally from this lattice, such that the energy minimum search is restricted to the *a priori* defined structural motifs.

Our algorithm successfully identifies previously reported high symmetry particles of all three structural motifs, indicating that the algorithm is stable and capable of identifying ground state structures. Interestingly, for single crystalline and decahedral particles our algorithm finds particles with energy on par with the energy of the magic number particles for *any* number of atoms. The primary reason is that both of these motifs provide ample opportunity for slight modifications of facet areas, shapes and asymmetries, which all have a very small impact on the total energy. For icosahedral particles, this is, however, not the case, since non-magic icosahedral particles are almost always stepped yielding an energy often substantially higher than the magic number particle energy.

The map of nanoparticle size to energy anywhere in the range from about 100 to 10,000 atoms is a first of its kind, and the paper concludes with a quantification of the

consequences for Ag, Au, Pd and Cu as calculated with EAM potentials. A Boltzmann distribution reveals that thermodynamic equilibrium ensembles almost always include more than one structural motif. The explanation is twofold. Firstly, the possibility to always find low energy single crystalline and decahedral particles render these two motifs energetically comparable in a wide size range. Secondly, and more importantly, the different particle sizes in a polydisperse ensemble will usually not all have the same ground state structural motif, since the rapid variations in ground state energy with particle size imply multiple crossovers in energy between the three motifs considered.

6.2 Paper II

In Paper II, the attention is turned to nanoalloys. Specifically, the paper contrasts the the chemical ordering in Au–Pd and Ag–Cu particles. The computational method is hybrid MD–MC simulations with energies calculated with EAM potentials. The paper focuses on results from simulated annealing, but simulations run at room temperature had practically identical results.

We invoke bulk-like interactions, surfaces and strain to explain differences in chemical ordering. Au–Pd mixes in all proportions in the bulk, whereas Ag–Cu has a wide miscibility gap. Our results indicate, as do the great majority of previous theoretical studies in the nanoalloy field, that this general mixing behavior is preserved at the nanoscale. There are, however, intriguing details at the atomic scale. For Au–Pd, where the surface energy differs substantially, the tendency of surface segregation is pronounced. The favorable Au–Pd bond, however, causes an excess of Pd in the subsurface layer, which can also be observed for flat surfaces. In the Ag–Cu system in which bonds between like bonds are favorable, there is no such enrichment in the subsurface layer. Although this observation may appear obvious, it is important to keep in mind for an experimentalist who measures surface composition with a technique that probes more than just the topmost surface layer.

Furthermore, the Au–Pd and Ag–Cu systems respond differently to strain. The increase in strain when going from a single crystalline particle to an icosahedron via a decahedron, provides an ideal playground to test this effect. Au–Pd has a small size mismatch and the difference in chemical ordering between the three motifs is consequently small. For Ag–Cu, however, which has a large size mismatch, there is a pronounced difference between the motifs. The arguably most intriguing consequence is the sequential filling of the tetrahedra in an icosahedron, which gives rise to a previously not reported sandwich-like structure at intermediate compositions.

Outlook

This thesis presents predictions of nanoparticle structures and chemical orderings in thermodynamic equilibrium. Even within this limited scope, there are a number of aspects that deserve increased attention in future studies.

From an experimental viewpoint it is problematic that all of the results are strictly valid only for particles suspended in vacuum. Nanoparticles in a laboratory are often stabilized by organic molecules, immersed in a liquid or gas and/or in contact with a substrate. The environment can rarely be accounted for easily but there are a number of methods that may prove useful in this regard. Particularly attractive for nanoalloys are cluster expansions [32, 33], which are lattice-based models that are usually fitted to DFT data. For reasonably well-behaved systems [93] they often reach an accuracy within 1–5 meV/atom from the corresponding DFT data [94, 95] and they thus provide an attractive substitute for interatomic potentials for predicting properties related to chemical ordering, especially given the relative simplicity of fitting a cluster expansion model [31]. Cluster expansions have successfully been used to study nanoparticles from several different perspectives, including equilibrium shape and chemical ordering with and without adsorbates [96, 97, 98, 99, 100, 101]. The algorithm of Paper I should be particularly well suited for adaptation to cluster expansion models instead of EAM potentials.

In addition to more realistic systems and elaborate computational methods, there is a need to further our understanding of how structure and chemical ordering impact the properties of nanoparticles. Nanoparticles are, for example, often used for heterogeneous catalysis and it is well established that both structure and chemical ordering can have a great impact on catalytic performance [83, 102, 103, 104]. It would be intriguing to couple the methods of this thesis to predictions of catalytic activity. Further, it would be interesting to use recently developed methods [105] to study the connection between chemical ordering and optical properties in general and generation of hot car-

riers in particular. Plasmonic sensing is yet another application for which alloying at the nanoscale is relevant and a better understanding may have an impact [106, 107].

There is apparently no lack of areas where the subjects of this thesis are of relevance, and hopefully the methods and results presented are merely a springboard to future insights, predictions and applications.

Decahedral and icosahedral geometry

Decahedra and icosahedra¹ can both be thought of as constructions based on, respectively, five and twenty triangular bipyramids. Since these bipyramids have edge lengths that are not all the same, they are not regular tetrahedra. When a decahedral or icosahedral particle is built with tetrahedra based on FCC crystals, the deviation from regular tetrahedral shape leads to strain. This appendix derives the ratios between the edge lengths in these shapes, which indicate what strain is geometrically required.

A.1 The decahedron

Consider a decahedron with edge lengths as defined in Fig. A.1. Pythagoras' theorem for the yellow face at the surface yields

$$\frac{x^2}{4} + b^2 = a^2. \quad (\text{A.1})$$

If we slice the decahedron through its equator, we obtain a new triangle with two sides of equal length (purple triangle in Fig. A.1). The angle at its top is $\theta = 2\pi/5$, so with c as the height of the triangle we may write

$$\tan \frac{\theta}{2} = \frac{x}{2c}. \quad (\text{A.2})$$

¹The terms decahedron and icosahedron are often used in a more general sense, referring to any polyhedron with ten or twenty faces. In this thesis, however, decahedron always refers to a pentagonal bipyramid and icosahedron to a regular icosahedron having equilaterally triangular faces.

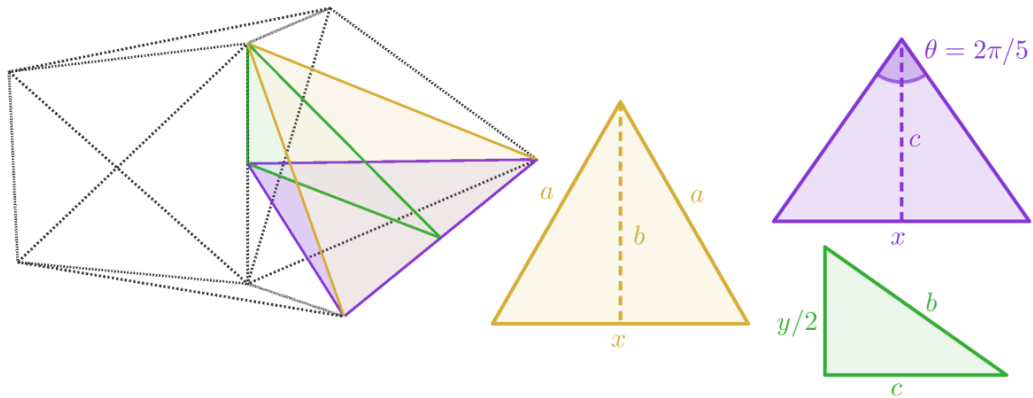


Figure A.1: Decahedron with variable definitions used in the text.

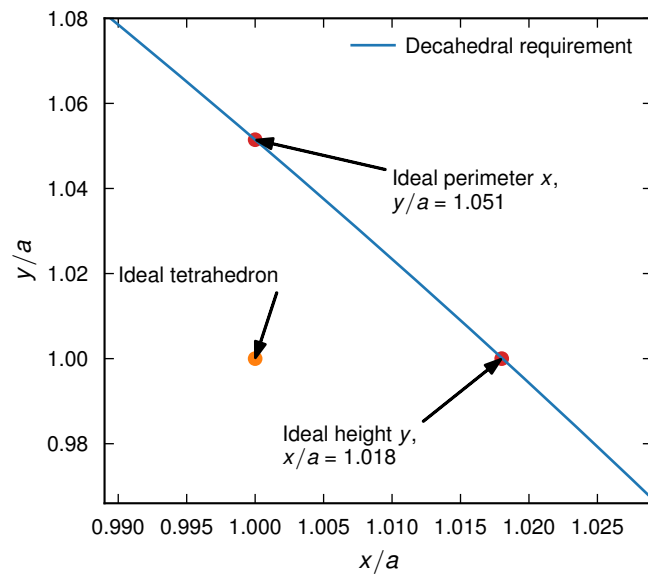


Figure A.2: Relation between edge length at the perimeter (x) and through the center (y) of a decahedron. Ideal tetrahedral geometry with all edges equally long (orange dot) is not possible.

We may now apply Pythagoras' theorem to the green triangle formed by the sides b , c and the edge in the center, the length of which is $y/2$,

$$\frac{y^2}{4} + c^2 = b^2. \quad (\text{A.3})$$

Putting the three equations together we find

$$y^2 + x^2 \left(1 + \frac{1}{\tan^2 \frac{\theta}{2}} \right) = 4a^2. \quad (\text{A.4})$$

With fixed a (essentially controlling the volume), we see that there is one degree of freedom; if x is chosen, y is determined and vice versa. This dependency precludes the possibility of regular tetrahedra (Fig. A.2). If the edge length in the center of the decahedron (y) is taken as ideal and identical to the edge lengths connecting the apex and the vertices at the equator (i.e., $y = a$), the edge lengths at the perimeter will be approximately 1.8 % longer than ideal ($x \approx 1.018a$).

A.2 The icosahedron

The twenty faces of an icosahedron can be viewed as the bases of triangular pyramids, the tips of which all meet in the center. For reasons of symmetry, the triangles on the faces are equilateral and the distances from the center to each vertex are identical. The question is thus what is the ratio between the edge length on the surface (a) and the radial edge length (b).

A derivation can be carried out conveniently by considering a path along the surface of the icosahedron, starting at a vertex and ending at the opposing vertex (purple line in Fig. A.3). If this path follows an edge and then the center of two triangular faces, the path lies in a plane. It encloses an area that can be split in three triangles with edge lengths easily determined from Pythagoras' theorem. It is also readily realized that some of the angles are the same. The law of cosines may be applied to the yellow and green triangles of Fig. A.3. For the yellow one we have

$$b^2 = a^2 + b^2 - 2ab \cos \theta \quad (\text{A.5})$$

so that

$$a = 2b \cos \theta. \quad (\text{A.6})$$

For the green triangle we have

$$\frac{3}{4}a^2 = b^2 + c^2 - 2bc \cos \theta. \quad (\text{A.7})$$

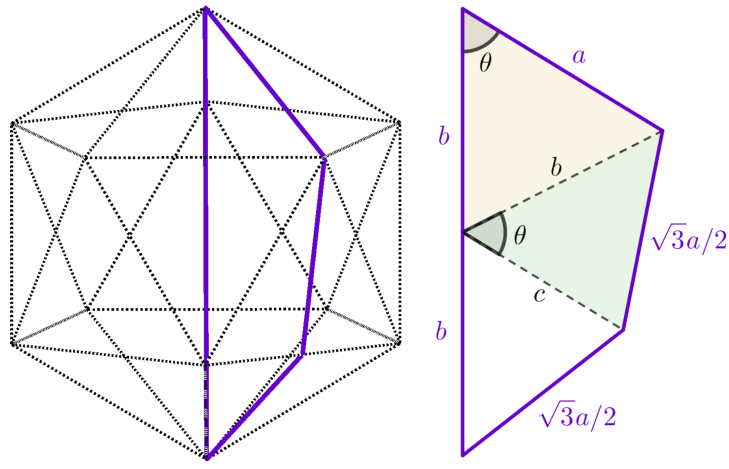


Figure A.3: Icosahedron with variable definitions used in the text.

By combining the two equations, we get

$$\frac{3}{4}a^2 = b^2 + c^2 - ac. \quad (\text{A.8})$$

The length c is obtained from Pythagoras' theorem,

$$c = \sqrt{b^2 - \frac{a^2}{4}} \quad (\text{A.9})$$

and by inserting this expression in Eq. (A.8) and squaring both sides, we obtain

$$5a^4 + 16b^4 - 20a^2b^2 = 0. \quad (\text{A.10})$$

Since we are deriving a relationship between a and b , we can write $b = \sqrt{k}a$ and the equation becomes

$$5 + 16k^2 - 20k = 0, \quad (\text{A.11})$$

which has (the relevant) solution

$$k = \frac{5 + \sqrt{5}}{8} \quad (\text{A.12})$$

so that

$$b = \sqrt{\frac{5 + \sqrt{5}}{8}}a \approx 0.951a. \quad (\text{A.13})$$

The radial edge length of an icosahedron is thus approximately 4.9% shorter than the edge length on the surface, or equivalently the edge length on the surface is approximately 5.1% longer than the radial edge length.

Acknowledgements

First, I want to thank Paul Erhart, my supervisor, for your unwavering encouragement, great enthusiasm, willingness to debate insignificant details, and for repeatedly providing convincing arguments for the existence of novelty in our work. Consider your aversion to certain high cultural expressions excused (for now).

Although the appended papers feature a minimal cast, there are many people who have indirectly contributed to this thesis and to whom I wish to extend my sincere gratitude.

Göran Wahnström, my examiner, for always providing support and for running the division in the best of ways.

Members of the Materials and Surface Theory division, current and former, for creating a great atmosphere at work and outside of work (I still do not like type hinting though).

Collaborators at the departments of physics and chemistry, for widening my views and for regularly providing irrefutable evidence that nanoparticles exist *ex silico*.

Family and friends, without whom this thesis may have appeared similar, but certainly not its author.

Bibliography

- [1] M. Faraday, X. *The Bakerian Lecture. —Experimental relations of gold (and other metals) to light*, Philosophical Transactions of the Royal Society of London **147**, 145 (1857).
- [2] L. Zhang, F. Gu, J. Chan, A. Wang, R. Langer, and O. Farokhzad, *Nanoparticles in Medicine: Therapeutic Applications and Developments*, Clinical Pharmacology & Therapeutics **83**, 761 (2008).
- [3] R. Müller, M. Radtke, and S. Wissing, *Solid lipid nanoparticles (SLN) and nanostructured lipid carriers (NLC) in cosmetic and dermatological preparations*, Advanced Drug Delivery Reviews **54**, S131 (2002).
- [4] M. F. L. De Volder, S. H. Tawfick, R. H. Baughman, and A. J. Hart, *Carbon Nanotubes: Present and Future Commercial Applications*, Science **339**, 535 (2013).
- [5] G. Wulff, *Zur Frage der Geschwindigkeit des Wachstums und der Auflösung der Krystallflächen*, Zeitschrift für Kristallographie **34**, 449 (1901).
- [6] L. Marks and L. Peng, *Nanoparticle shape, thermodynamics and kinetics*, Journal of Physics: Condensed Matter **28**, 053001 (2016).
- [7] J. Löfgren, Licentiate thesis, Department of Physics, Chalmers University of Technology, 2017.
- [8] Y. Mishin, M. J. Mehl, D. A. Papaconstantopoulos, A. F. Voter, and J. D. Kress, *Structural stability and lattice defects in copper: Ab initio, tight-binding, and embedded-atom calculations*, Physical Review B **63**, 224106 (2001).
- [9] P. L. Williams, Y. Mishin, and J. C. Hamilton, *An embedded-atom potential for the Cu-Ag system*, Modelling and Simulation in Materials Science and Engineering **14**, 817 (2006).
- [10] R. Marchal, A. Genest, S. Krüger, and N. Rösch, *Structure of Pd/Au Alloy Nanoparticles from a Density Functional Theory-Based Embedded-Atom Potential*, The Journal of Physical Chemistry C **117**, 21810 (2013).

Bibliography

- [11] A. Patra, J. E. Bates, J. Sun, and J. P. Perdew, *Properties of real metallic surfaces: Effects of density functional semilocality and van der Waals nonlocality*, Proceedings of the National Academy of Sciences **114**, E9188 (2017).
- [12] J. P. Perdew, K. Burke, and M. Ernzerhof, *Generalized gradient approximation made simple*, Physical Review Letters **77**, 3865 (1996), erratum, *ibid.* **78**, 1396(E) (1997).
- [13] S. Zhou, M. Zhao, T.-H. Yang, and Y. Xia, *Decahedral nanocrystals of noble metals: Synthesis, characterization, and applications*, Materials Today, in press.
- [14] S. Ino, *Epitaxial Growth of Metals on Rocksalt Faces Cleaved in Vacuum. II. Orientation and Structure of Gold Particles Formed in Ultrahigh Vacuum*, Journal of the Physical Society of Japan **21**, 346 (1966).
- [15] S. Ino and S. Ogawa, *Multiply Twinned Particles at Earlier Stages of Gold Film Formation on Alkali Halide Crystals*, Journal of the Physical Society of Japan **22**, 1365 (1967).
- [16] L. D. Marks, *Modified Wulff constructions for twinned particles*, Journal of Crystal Growth **61**, 556 (1983).
- [17] L. D. Marks, *Surface structure and energetics of multiply twinned particles*, Philosophical Magazine A **49**, 81 (1984).
- [18] D. J. Smith and L. Marks, *High resolution studies of small particles of gold and silver: II. Single crystals, lamellar twins and polyparticles*, Journal of Crystal Growth **54**, 433 (1981).
- [19] G. Rossi, A. Rapallo, C. Mottet, A. Fortunelli, F. Baletto, and R. Ferrando, *Magic Polyicosahedral Core-Shell Clusters*, Physical Review Letters **93**, 105503 (2004).
- [20] K. Kimoto and I. Nishida, *An electron microscope and electron diffraction study of fine smoke particles prepared by evaporation in argon gas at low pressures (II)*, Japanese Journal of Applied Physics **6**, 1047 (1967).
- [21] M. Grzelczak, J. Pérez-Juste, P. Mulvaney, and L. M. Liz-Marzán, *Shape control in gold nanoparticle synthesis*, Chemical Society Reviews **37**, 1783 (2008).
- [22] Y. Sun and Y. Xia, *Shape-Controlled Synthesis of Gold and Silver Nanoparticles*, Science **298**, 2176 (2002).
- [23] T. K. Sau and C. J. Murphy, *Room Temperature, High-Yield Synthesis of Multiple Shapes of Gold Nanoparticles in Aqueous Solution*, Journal of the American Chemical Society **126**, 8648 (2004).

-
- [24] N. R. Jana, L. Gearheart, and C. J. Murphy, *Seed-Mediated Growth Approach for Shape-Controlled Synthesis of Spheroidal and Rod-like Gold Nanoparticles Using a Surfactant Template*, *Advanced Materials* **13**, 1389 (2001).
- [25] S. E. Skrabalak, J. Chen, Y. Sun, X. Lu, L. Au, C. M. Cobley, and Y. Xia, *Gold Nanocages: Synthesis, Properties, and Applications*, *Accounts of Chemical Research* **41**, 1587 (2008).
- [26] F. Baletto, R. Ferrando, A. Fortunelli, F. Montalenti, and C. Mottet, *Crossover among structural motifs in transition and noble-metal clusters*, *The Journal of Chemical Physics* **116**, 3856 (2002).
- [27] K. P. McKenna, *Gold nanoparticles under gas pressure*, *Physical Chemistry Chemical Physics* **11**, 4145 (2009).
- [28] A. S. Barnard, N. P. Young, A. I. Kirkland, M. A. van Huis, and H. Xu, *Nanogold: A Quantitative Phase Map*, *ACS Nano* **3**, 1431 (2009).
- [29] H. Li, L. Li, A. Pedersen, Y. Gao, N. Khetrpal, H. Jónsson, and X. C. Zeng, *Magic-number gold nanoclusters with diameters from 1 to 3.5 nm: Relative stability and catalytic activity for CO oxidation*, *Nano Letters* **15**, 682 (2015).
- [30] S. Plimpton, *Fast Parallel Algorithms for Short-Range Molecular Dynamics*, *Journal of Computational Physics* **117**, 1 (1995).
- [31] M. Ångqvist, W. A. Muñoz, J. M. Rahm, E. Fransson, C. Durniak, P. Rozyczko, T. H. Rod, and P. Erhart, *ICET – A Python library for constructing and sampling alloy cluster expansions*, arXiv:1901.08790.
- [32] J. Sanchez, F. Ducastelle, and D. Gratias, *Generalized cluster description of multicomponent systems*, *Physica A: Statistical Mechanics and its Applications* **128**, 334 (1984).
- [33] D. de Fontaine, in *Solid State Physics*, edited by H. Ehrenreich and D. Turnbull (Academic Press, New York, 1994), Vol. 47, p. 33.
- [34] G. L. W. Hart, *Where are nature's missing structures?*, *Nature Materials* **6**, 941 (2007).
- [35] W. Hume-Rothery, Ph.D. thesis, University of London, 1926.
- [36] J. C. Slater, *Atomic Radii in Crystals*, *The Journal of Chemical Physics* **41**, 3199 (1964).
- [37] A. Allred, *Electronegativity values from thermochemical data*, *Journal of Inorganic and Nuclear Chemistry* **17**, 215 (1961).

Bibliography

- [38] H. Okamoto, M. Schlesinger, and E. Mueller, *Alloy Phase Diagrams* (ASM International, Materials Park, Ohio, 2016), Vol. 3.
- [39] J. Pohl, C. Stahl, and K. Albe, *Size-dependent phase diagrams of metallic alloys: A Monte Carlo simulation study on order-disorder transitions in Pt-Rh nanoparticles*, *Beilstein Journal of Nanotechnology* **3**, 1 (2012).
- [40] G. Guisbiers, R. Mendoza-Cruz, L. Bazán-Díaz, J. J. Velázquez-Salazar, R. Mendoza-Perez, J. A. Robledo-Torres, J. L. Rodríguez-Lopez, J. M. Montejano-Carrizales, R. L. Whetten, and M. José-Yacamán, *Electrum, the gold-silver alloy, from the bulk scale to the nanoscale: Synthesis, properties, and segregation rules*, *ACS Nano* **10**, 188 (2016).
- [41] G. Guisbiers, S. Mejia-Rosales, S. Khanal, F. Ruiz-Zepeda, R. L. Whetten, and M. José-Yacamán, *Gold-Copper Nano-Alloy, "Tumbaga", in the Era of Nano: Phase Diagram and Segregation*, *Nano Letters* **14**, 6718 (2014).
- [42] G. Guisbiers, R. Mendoza-Pérez, L. Bazán-Díaz, R. Mendoza-Cruz, J. J. Velázquez-Salazar, and M. José-Yacamán, *Size and Shape Effects on the Phase Diagrams of Nickel-Based Bimetallic Nanoalloys*, *The Journal of Physical Chemistry C* **121**, 6930 (2017).
- [43] M. Fèvre, Y. Le Bouar, and A. Finel, *Thermodynamics of phase-separating nanoalloys: Single particles and particle assemblies*, *Physical Review B* **97**, 195404 (2018).
- [44] Y. Yang, C.-c. Chen, M. C. Scott, C. Ophus, R. Xu, A. P. Jr, L. Wu, F. Sun, W. Theis, J. Zhou, M. Eisenbach, P. R. C. Kent, R. F. Sabirianov, H. Zeng, P. Ercius, and J. Miao, *Deciphering chemical order/disorder and material properties at the single-atom level*, *Nature* **542**, 75 (2017).
- [45] A. Christensen, P. Stoltze, and J. K. Norskov, *Size dependence of phase separation in small bimetallic clusters*, *Journal of Physics: Condensed Matter* **7**, 1047 (1995).
- [46] Y. Dahan, G. Makov, and R. Shneck, *Nanometric size dependent phase diagram of Bi-Sn*, *Calphad* **53**, 136 (2016).
- [47] J. Luo, M. M. Maye, V. Petkov, N. N. Kariuki, L. Wang, P. Njoki, D. Mott, Y. Lin, and C.-J. Zhong, *Phase Properties of Carbon-Supported Gold-Platinum Nanoparticles with Different Bimetallic Compositions*, *Chemistry of Materials* **17**, 3086 (2005).
- [48] J. Luo, P. N. Njoki, Y. Lin, D. Mott, Wang, and C.-J. Zhong, *Characterization of Carbon-Supported AuPt Nanoparticles for Electrocatalytic Methanol Oxidation Reaction*, *Langmuir* **22**, 2892 (2006).

-
- [49] M. Schrunner, S. Proch, Y. Mei, R. Kempe, N. Miyajima, and M. Ballauff, *Stable Bimetallic Gold–Platinum Nanoparticles Immobilized on Spherical Polyelectrolyte Brushes: Synthesis, Characterization, and Application for the Oxidation of Alcohols*, *Advanced Materials* **20**, 1928 (2008).
- [50] O. Malis, M. Radu, D. Mott, B. Wanjala, J. Luo, and C. Zhong, *An in situ real-time x-ray diffraction study of phase segregation in Au–Pt nanoparticles*, *Nanotechnology* **20**, 245708 (2009).
- [51] V. Petkov, B. N. Wanjala, R. Loukrakpam, J. Luo, L. Yang, C.-J. Zhong, and S. Shastri, *Pt–Au Alloying at the Nanoscale*, *Nano Letters* **12**, 4289 (2012).
- [52] L. Leppert, R. Q. Albuquerque, and S. Kümmel, *Gold–platinum alloys and Vegard’s law on the nanoscale*, *Physical Review B* **86**, 241403 (2012).
- [53] M. Chatzidakis, S. Prabhudev, P. Saidi, C. N. Chiang, J. J. Hoyt, and G. A. Botton, *Bulk Immiscibility at the Edge of the Nanoscale*, *ACS Nano* **11**, 10984 (2017).
- [54] J.-P. Palomares-Baez, E. Panizon, and R. Ferrando, *Nanoscale Effects on Phase Separation*, *Nano Letters* **17**, 5394 (2017).
- [55] H. B. Callen, *Thermodynamics and an Introduction to Thermostatistics*, 2 ed. (Wiley, New York, 1985).
- [56] T. L. Hill, *Thermodynamics of Small Systems* (W.A. Benjamin, New York, 1963, 1964), Vol. 1, 2.
- [57] J. Dunkel and S. Hilbert, *Consistent thermostatistics forbids negative absolute temperatures*, *Nature Physics* **10**, 67 (2013).
- [58] D. Frenkel and P. B. Warren, *Gibbs, Boltzmann, and negative temperatures*, *American Journal of Physics* **83**, 163 (2015).
- [59] R. H. Swendsen, *Thermodynamics of finite systems: a key issues review*, *Reports on Progress in Physics* **81**, 072001 (2018).
- [60] F. Calvo, *Thermodynamics of nanoalloys*, *Physical Chemistry Chemical Physics* **17**, 27922 (2015).
- [61] P. Buffat and J.-P. Borel, *Size effect on the melting temperature of gold particles*, *Physical Review A* **13**, 2287 (1976).
- [62] E. B. Tadmor and R. E. Miller, *Modeling Materials: Continuum, Atomistic and Multiscale Techniques* (Cambridge University Press, Cambridge, England, 2011).

Bibliography

- [63] M. S. Daw, S. M. Foiles, and M. I. Baskes, *The embedded-atom method: a review of theory and applications*, Materials Science Reports **9**, 251 (1993).
- [64] M. S. Daw and M. I. Baskes, *Embedded-atom method: Derivation and application to impurities, surfaces, and other defects in metals*, Physical Review B **29**, 6443 (1984).
- [65] J. K. Nørskov and N. D. Lang, *Effective-medium theory of chemical binding: Application to chemisorption*, Physical Review B **21**, 2131 (1980).
- [66] K. W. Jacobsen, J. K. Nørskov, and M. J. Puska, *Interatomic interactions in the effective-medium theory*, Physical Review B **35**, 7423 (1987).
- [67] M. W. Finnis and J. E. Sinclair, *A simple empirical N-body potential for transition metals*, Philosophical Magazine A **50**, 45 (1984).
- [68] F. Ercolessi, E. Tosatti, and M. Parrinello, *Au (100) Surface Reconstruction*, Physical Review Letters **57**, 719 (1986).
- [69] P. Hohenberg and W. Kohn, *Inhomogeneous Electron Gas*, Physical Review **136**, B864 (1964).
- [70] M. J. Stott and E. Zaremba, *Quasiatoms: An approach to atoms in nonuniform electronic systems*, Physical Review B **22**, 1564 (1980).
- [71] N. Metropolis, A. W. Rosenbluth, M. N. Rosenbluth, A. H. Teller, and E. Teller, *Equation of State Calculations by Fast Computing Machines*, The Journal of Chemical Physics **21**, 1087 (1953).
- [72] B. Sadigh and P. Erhart, *Calculation of excess free energies of precipitates via direct thermodynamic integration across phase boundaries*, Physical Review B **86**, 134204 (2012).
- [73] B. Sadigh, P. Erhart, A. Stukowski, A. Caro, E. Martinez, and L. Zepeda-Ruiz, *Scalable parallel Monte Carlo algorithm for atomistic simulations of precipitation in alloys*, Physical Review B **85**, 184203 (2012).
- [74] S. M. Woodley and R. Catlow, *Crystal structure prediction from first principles*, Nature materials **7**, 937 (2008).
- [75] S. Heiles and R. L. Johnston, *Global optimization of clusters using electronic structure methods*, International Journal of Quantum Chemistry **113**, 2091 (2013).
- [76] M. Jäger, R. Schäfer, and R. L. Johnston, *First principles global optimization of metal clusters and nanoalloys*, Advances in Physics: X **3**, 1516514 (2018).

-
- [77] I. L. Garzón, K. Michaelian, M. R. Beltrán, A. Posada-Amarillas, P. Ordejón, E. Artacho, D. Sánchez-Portal, and J. M. Soler, *Lowest Energy Structures of Gold Nanoclusters*, *Physical Review Letters* **81**, 1600 (1998).
- [78] R. L. Johnston, *Evolving better nanoparticles: Genetic algorithms for optimising cluster geometries*, *Dalton Transactions* **22**, 4193 (2003).
- [79] D. J. Wales and J. P. Doye, *Global optimization by basin-hopping and the lowest energy structures of Lennard-Jones clusters containing up to 110 atoms*, *The Journal of Physical Chemistry A* **101**, 5111 (1997).
- [80] E. Aprà, R. Ferrando, and A. Fortunelli, *Density-functional global optimization of gold nanoclusters*, *Physical Review B* **73**, 205414 (2006).
- [81] X. Chen, Y.-F. Zhao, L.-S. Wang, and J. Li, *Recent progresses of global minimum searches of nanoclusters with a constrained Basin-Hopping algorithm in the TGMIn program*, *Computational and Theoretical Chemistry* **1107**, 57 (2017).
- [82] S. Darby, T. V. Mortimer-Jones, R. L. Johnston, and C. Roberts, *Theoretical study of Cu–Au nanoalloy clusters using a genetic algorithm*, *The Journal of Chemical Physics* **116**, 1536 (2002).
- [83] R. Ferrando, J. Jellinek, and R. L. Johnston, *Nanoalloys: From Theory to Applications of Alloy Clusters and Nanoparticles*, *Chemical Reviews* **108**, 845 (2008).
- [84] N. Zhang, F. Chen, and X. Wu, *Global optimization and oxygen dissociation on polyicosahedral Ag₃₂Cu₆ core-shell cluster for alkaline fuel cells*, *Scientific reports* **5**, 11984 (2015).
- [85] D. Rapetti and R. Ferrando, *Density functional theory global optimization of chemical ordering in AgAu nanoalloys*, *Journal of Alloys and Compounds* **779**, 582 (2019).
- [86] P. M. Larsen, K. W. Jacobsen, and J. Schiøtz, *Rich Ground-State Chemical Ordering in Nanoparticles: Exact Solution of a Model for Ag–Au Clusters*, *Physical Review Letters* **120**, 256101 (2018).
- [87] R. Ferrando, *Symmetry breaking and morphological instabilities in core-shell metallic nanoparticles*, *Journal of Physics: Condensed Matter* **27**, 013003 (2014).
- [88] K. Laasonen, E. Panizon, D. Bochicchio, and R. Ferrando, *Competition between Icosahedral Motifs in AgCu, AgNi, and AgCo Nanoalloys: A Combined Atomistic–DFT Study*, *The Journal of Physical Chemistry C* **117**, 26405 (2013).

Bibliography

- [89] G. Kovács, S. M. Kozlov, and K. M. Neyman, *Versatile Optimization of Chemical Ordering in Bimetallic Nanoparticles*, *The Journal of Physical Chemistry C* **121**, 10803 (2017).
- [90] J. F. Nye, *Physical properties of crystals: their representation by tensors and matrices* (Oxford university press, Oxford, 1985).
- [91] A. Stukowski, *Visualization and analysis of atomistic simulation data with OVITO—the Open Visualization Tool*, *Modelling and Simulation in Materials Science and Engineering* **18**, 015012 (2009).
- [92] A. Stukowski, *Structure identification methods for atomistic simulations of crystalline materials*, *Modelling and Simulation in Materials Science and Engineering* **20**, 045021 (2012).
- [93] A. H. Nguyen, C. W. Rosenbrock, C. S. Reese, and G. L. W. Hart, *Robustness of the cluster expansion: Assessing the roles of relaxation and numerical error*, *Physical Review B* **96**, 014107 (2017).
- [94] L. J. Nelson, V. Ozoliņš, C. S. Reese, F. Zhou, and G. L. W. Hart, *Cluster expansion made easy with Bayesian compressive sensing*, *Physical Review B* **88**, 155105 (2013).
- [95] M. Ångqvist and P. Erhart, *Understanding Chemical Ordering in Intermetallic Clathrates from Atomic Scale Simulations*, *Chemistry of Materials* **29**, 7554 (2017).
- [96] T. Mueller and G. Ceder, *Effect of Particle Size on Hydrogen Release from Sodium Alanate Nanoparticles*, *ACS Nano* **4**, 5647 (2010).
- [97] R. V. Chepulskii, W. Butler, A. van de Walle, and S. Curtarolo, *Surface segregation in nanoparticles from first principles: The case of FePt*, *Scripta Materialia* **62**, 179 (2010).
- [98] L.-L. Wang, T. L. Tan, and D. D. Johnson, *Configurational Thermodynamics of Alloyed Nanoparticles with Adsorbates*, *Nano Letters* **14**, 7077 (2014).
- [99] J. Teeriniemi, M. Melander, S. Lipasti, R. Hatz, and K. Laasonen, *Fe–Ni Nanoparticles: A Multiscale First-Principles Study to Predict Geometry, Structure, and Catalytic Activity*, *The Journal of Physical Chemistry C* **121**, 1667 (2017).
- [100] L. Cao, C. Li, and T. Mueller, *The Use of Cluster Expansions To Predict the Structures and Properties of Surfaces and Nanostructured Materials*, *Journal of Chemical Information and Modeling* **58**, 2401 (2018).

-
- [101] C. Li, D. Raciti, T. Pu, L. Cao, C. He, C. Wang, and T. Mueller, *Improved Prediction of Nanoalloy Structures by the Explicit Inclusion of Adsorbates in Cluster Expansions*, *The Journal of Physical Chemistry C* **122**, 18040 (2018).
- [102] M. Melander, V. Latsa, and K. Laasonen, *CO dissociation on iron nanoparticles: Size and geometry effects*, *The Journal of Chemical Physics* **139**, 164320 (2013).
- [103] L. Liu and A. Corma, *Metal Catalysts for Heterogeneous Catalysis: From Single Atoms to Nanoclusters and Nanoparticles*, *Chemical Reviews* **118**, 4981 (2018).
- [104] T. N. Pingel, M. Jørgensen, A. B. Yankovich, H. Grönbeck, and E. Olsson, *Influence of atomic site-specific strain on catalytic activity of supported nanoparticles*, *Nature communications* **9**, 2722 (2018).
- [105] T. P. Rossi, M. Kuisma, M. J. Puska, R. M. Nieminen, and P. Erhart, *Kohn–Sham Decomposition in Real-Time Time-Dependent Density-Functional Theory: An Efficient Tool for Analyzing Plasmonic Excitations*, *Journal of Chemical Theory and Computation* **13**, 4779 (2017).
- [106] C. Wadell, F. A. A. Nugroho, E. Lidström, B. Iandolo, J. B. Wagner, and C. Langhammer, *Hysteresis-Free Nanoplasmonic Pd–Au Alloy Hydrogen Sensors*, *Nano Letters* **15**, 3563 (2015).
- [107] F. A. A. Nugroho, I. Darmadi, V. P. Zhdanov, and C. Langhammer, *Universal Scaling and Design Rules of Hydrogen-Induced Optical Properties in Pd and Pd-Alloy Nanoparticles*, *ACS Nano* **12**, 9903 (2018).